FERMILAB-CONF-75-122-E #98

EFI 75-46

High Energy Muon Scatterings at Fermilab/Serpukhov

Luke W. Mo

Enrico Fermi Institute and Department of Physics
The University of Chicago
Chicago, Illinois 60637, U.S.A.

(Rapporteur's talk presented at the 1975 International Symposium on Lepton and Photon Interactions at High Energies, Stanford University, Stanford, California, August 21-27, 1975)

CONTENTS

I. Introduction

II. Muon Beam at Fermilab

III. Test of Bjorken Scaling

(A) Experimental Results on Scaling

(B) Comparison with a Monte Carlo Calculation

IV. Muon Scatterings from Hydrogen and Deuterium

A. The Experimental Apparatus

B. Data Analysis

C. Results on νW_2

D. Results on Hadron Distributions

1. The $P_\perp^2$-Distributions

2. The P_n-Distributions

3. The Missing Mass Spectra and t-Distributions

4. The Charge Ratio

5. The $x_\parallel$-Distributions

V. Search for Parity Non-Conservation Effects in Deep Inelastic μN Interactions

Acknowledgements

Table I

Table II

Appendix

References

Figure Captions

High Energy Muon Scatterings at Fermilab/Serpukhov

I. Introduction

Exactly two decades ago, Panofsky and his collaborators started to do inelastic scattering experiment with high energy electrons.[1] The first result on the electroproduction of (33) resonance is shown in Figure 1.[2] Theoretical work on this subject was done by Dalitz and Yennie,[3] and by Fubini, Nambu, and Wataghin.[4]

The most important development after these pioneer works has been the discovery of the Bjorken scaling at SLAC by a MIT-SLAC collaboration.[5,6] It has initiated a tremendous amount of activities, both experimental[7] and theoretical,[8] on the study of the so called "deep inelastic scattering" phenomena.

It is apparently true that the most pressing question in high energy physics is still "what is the nucleon made of"? Traditionally, experiments with high energy electrons can always provide good, if still incomplete, answers to this difficult problem. Because of the lack of an expensive electron accelerator in the multi-hundred GeV range, it is natural to continue the study with high energy muons at Fermilab. The muon is capable of producing virtual photons, which probe the target nucleons, exactly as the electron does. Even though the beam intensity is much lower and phase space bigger, very interesting physics can still be done successfully with a muon beam of modest intensity in kinematical regions unexplored before.

Two muon scattering experiments were carried out at Fermilab: one is

on the test of Bjorken scaling with an iron target; and the other on the muon scatterings from a liquid hydrogen/deuterium target. In the following sections, their results will be presented in turn after a brief description of the Fermilab muon beam. Then the results from a lower energy experiment performed at Serpukhov, U.S.S.R., on the study of parity violation effects in deep inelastic μN scatterings, will be reported.

II. The Muon Beam at Fermilab

The schematic layout of the muon beam at Fermilab is shown in Figure 2. Its beam optics is shown in Figure 3. The pions and kaons produced at the production target are first focused by a quadrupole triplet. The decay muons are focused by three quadrupole doublets onto the experimental target. At the intermediate focal point, approximately 40' of CH_2 is inserted in the beamline to remove the hadrons from the muon beam.

The yield of positive muons on target is approximately 10^{-7} per incident primary proton. For negative muons, the yield is about a factor of three lower. The muon intensity becomes optimum when its operating energy is approximately half that of the primary protons. For most of the experimental runs, the useful positive muon intensity was $\sim 10^6$ per pulse. The momentum acceptance of the muon beam is typically ±2.5%. Since the pion decay can only give a transverse momentum of 30 MeV/c, most of the muons are concentrated in the forward direction, and confined in an area of ~5" in diameter at the target position. The halo was feared, but it has not constituted a problem to the experiments at the present level of beam intensity.

III. Test of Bjorken Scaling

In a high energy muon scattering experiment, conducted by a Cornell-Michigan State-Berkeley-La Jolla collaboration,[9] the scale invariance is directly tested by a ratio method which compares the muon scattering cross sections from an iron target at two different incident muon energies. The principle of this experiment can be easily understood by parametrizing the muon scattering cross section at small angles as

$$E\frac{d^2\sigma}{dxdy} = \frac{4\pi\alpha^2}{2M}\frac{(\nu W_2)}{x^2y^2}[1 - y + y^2/2(1 + R)],$$

where $\nu = E-E'$, $x = \frac{q^2}{2M\nu}$, $y = \frac{\nu}{E}$, and $R = \frac{\sigma_L}{\sigma_t}$. The symbols are defined as: E, the incident muon energy; E', the scattered muon energy; q^2, the 4-momentum transfer squared; M, the nucleon mass; σ_L and σ_t, the longitudinal and transverse virtual photoproduction cross section as defined by Hand.[10] If the following scale transformation is made:

$E \rightarrow \lambda E$ (change the incident energy by a factor of λ),

$E' \rightarrow \lambda E'$ (change the magnetic spectrometer setting by a factor of λ),

$\theta \rightarrow \frac{1}{\sqrt{\lambda}}\theta$ (change the target-spectrometer distance by a factor of $\frac{1}{\sqrt{\lambda}}$).

Then one will have $\nu \rightarrow \lambda\nu$, $q^2 \rightarrow \lambda q^2$, but ω remains unchanged. The ratio of the cross sections at two different incident muon energies, defined by

$$r(\omega,q^2) \equiv \frac{[E \frac{d^2\sigma}{dxdy}]_{E = \lambda E_0}}{[E \frac{d^2\sigma}{dxdy}]_{E = E_0}}$$

will remain constant at all values of ω and q^2 if the Bjorken scale invariance continues to be valid.

The experimental apparatus is shown in Figure 4. The spectrometer is made mainly of magnetized iron toroids and wire spark chambers. The kinematical region it can cover is shown in Figure 5. The measurements were done at incident muon energies of 150 GeV and 56 GeV (λ = 8/3). The target was also scaled, 622 gm/cm^2 at 150 GeV and 233 gm/cm^2 at 56 GeV, to give equal counting rate per incident muon.

(A) Experimental Results on Scaling

The values of $r(\omega,q^2)$, measured with 1.5 X 10^9 μ^+ at 150 GeV and 4 X 10^9 μ^+ at 56 GeV, is shown in Figure 6. The result had been corrected for experimental non-scaling effects such as (1) different radial distributions of the beam, (2) inexact scaling of spectrometer resolution and acceptance, and (3) radiative corrections.

The obvious conclusion one can draw from these results is that scale non-invariance has been observed.

(B) Comparison with a Monte Carlo Calculation

The same collaboration also compared their measured cross sections with a scale-invariant Monte Carlo calculation, using the νW_2 function measured at SLAC as input. The iron target was treated as a collection of nucleons in Fermi motion. A variety of experimental effects, such as radiative corrections, multiple Coulomb scatterings, μe scatterings, muon bremsstrahlung, muon energy loss in the magnetized iron toroid, miss-measurements by wire chambers, etc., were all folded in. Ratios of observed to simulated event rates are shown in Figure 7. These plots indicate a distinctive feature that the deviation from Bjorken scaling as a function of q^2 has a negative slope at values of ω less than 5; and this slope becomes positive at values of ω greater than 5. This phenomenon seems to be in accord with the prediction of Tung,[11] using conventional field theory and also asymptotic freedom theory with anomalous dimensions. This particular calculation says that at large values of ω, νW_2 should first rise and then fall as q^2 increases; at values of ω less than 5, νW_2 should continue to decrease as q^2 increases.

Vector-dominance models or generalized vector-dominance models also predicted the increase of νW_2 with q^2.[12,13,14]

In the parton model of Drell and Chanowitz[15] the scaling violation is exhibited through the introduction of a parton form factor.

Now we are facing a very interesting situation. The scale invariance is totally violated in the time-like region.[16] In the space-like region,

this muon experiment at Fermilab indicated a violation of Bjorken scaling at a level of only less than ~30%. This fact alone should provide enough incentives to continue the study at higher energies.

IV. Muon Scatterings from Hydrogen and Deuterium

The experiment on muon scatterings from a liquid hydrogen or deuterium target was carried out at Fermilab by a Chicago-Harvard -Illinois-Oxford collaboration.[17] The aim of the experiment is to measure the inclusive muon cross sections for the evaluation of nucleon structure functions, and also the hadron distributions in muo-production. As the result of the experiment is not yet available, we will briefly describe first the apparatus, and then the analysis problem and the preliminary results.

A. The Experimental Apparatus

The central element of the spectrometer is a large volume magnet, the Chicago Cyclotron, on which the (33) resonance was discovered.[18] The layout of the spectrometer is shown in Figure 8. The incoming muon beam was first measured, before and after a tagging magnet, by six sets of scintillation hodoscopes and beam chambers before it reached the liquid target. The unscattered muon beam was vetoed by a scintillation hodoscope (N) downstream of the Cyclotron magnet and apparatus. The halo muons was vetoed by a large size scintillation hodoscope in front of the target. There were two banks of horizontal and vertical scintillation hodoscopes (G and H) installed before an 8' thick steel hadron absorber; and two more banks (M and M') behind the absorber. The scattered muon was recognized by its unique ability to penetrate the 8' thick steel shield, and by its changing of

directions from the beam. The master trigger of the experiment was defined by the requirement of the logic: Beam * $\overline{\text{Halo}}$ * (G.OR.H) * (M.OR.M') * $\overline{\text{N}}$. It meant: There was an incident muon, the halo counter was not set, G or H fired, M or M' fired, and the downstream beam veto N was not set. For a typical 150 GeV run, the trigger rate was ~8 per pulse, with a random coincidence rate of ~15%.

The liquid target was contained in a flask, 48" long and 7" in diameter. Upon occurence of a trigger, all detector information was strobed into an on-line XDS Σ-3 computer and logged onto magnetic tapes. There were on-line programs for equipment monitoring, but no attempt was made to do on-line physics analysis.

B. Data Analysis

In the off-line data analysis, pattern recognitions were first done separately for tracks in the beam MWPC's, tracks in the 1m X 1m MWPC's between the target and the Cyclotron magnet, and the tracks in the wire spark chambers downstream of the Cyclotron magnet. These tracks were then masked by the scintillation hodoscopes to filter out the out-of-time ones, particularly those stale tracks found in the wire spark chambers. A typical muon scattering event is shown in Figure 9. The momentum determination of the beam was trivial. The muo-produced tracks were handled in the following manner:

1. In the non-bending view, the tracks downstream and upstream of the magnet were linked by demanding they should have the same slope and intercept at the middle of the magnet.

2. In the bending view, the tracks were linked by demanding that they should have the same impact parameter with respect to the center of the Cyclotron magnet.

Once the track was found, the momentum was then calculated with a hard-edged field distribution and an appropriate effective radius.

The acceptance of the scattered muon can be calculated in a variety of ways. One way to do it was to rotate the outgoing muon momentum vector around the incoming muon momentum vector. This whole cone was tracked through the Cyclotron magnet and then the acceptance was determined by the sizes of the hodoscopes. This method automatically folds in the radial distributions of the beam. Another way to do it was to do a pre-calculation using Monte Carlo technique and then interpolate.

For the hadrons, the acceptance was calculated by assuming the incoming beam was the virtual photon. Then the acceptance can be calculated easily by rotating the hadron momentum vector around the virtual photon momentum vector. The boundary of the acceptance was determined by the sizes of G and H hodoscopes.

Cross section for the scattered muons were calculated from the following relation

$$\frac{d^2\sigma}{dq^2 d\nu} = \frac{N_{bin}\, C}{N_\mu\, N_T\, (\Delta q^2\, \Delta\nu)\, A_\mu}$$

where

N_{bin} is the number of scattered muons accepted in a given $(\Delta q^2 \Delta\nu)$ bin.

$N\mu$ is the total number of incident muons.

N_T is the number of target nucleons/cm^2.

A_μ is the acceptance of the scattered muons in the $(\Delta q^2 \Delta\nu)$ bin.

C is to allow for several corrections to the data. The important ones were the radiative corrections, equipment dead-time corrections, and counter efficiencies.

Cross sections for hadron distributions were evaluated in the same manner. The only difference was that acceptances and corrections had to be taken into account for both hadrons and the scattered muon.

C. Results on νW_2

Data had been taken with 150 GeV μ^+ on liquid hydrogen and liquid deuterium; also with 100 GeV μ^+ on liquid hydrogen. We present here the preliminary result based on ~250,000 triggers of 150 GeV μ^+ on liquid deuterium and also approximately the same amount of triggers of 150 GeV μ^+ on liquid hydrogen. The kinematical region covered by this experiment is shown in Figure 10. The number of scattered muon events found is ~60,000 on LD_2 and ~30,000 on LH_2; most of them are clustered around low q^2 and high ν regions. In Figure 10, the shaded area contains a low number

of counts which was not included yet in the results presented here. The region of q^2 values between 0 and 3 $(GeV/c)^2$ and values of ν between 0 and 90 GeV was also excluded, because the beam veto (N) made the acceptance negligible in this area.

The radiative corrections [19,20] were done by first calculating a ratio defined by the following expression for proton,

$$\delta_R = \frac{\sigma^{inelastic}}{\sigma^{inelastic}_{radiated} + \sigma^{P}_{tail}} ;$$

and for deuterium,

$$\delta_R = \frac{\sigma^{inelastic}}{\sigma^{inelastic}_{radiated} + \sigma^{Quasi}_{tail} + \sigma^{D}_{tail}} ;$$

where $\sigma^{inelastic}$ is the inelastic cross section calculated with the known νW_2 function together with its q^2-dependence; $\sigma^{inelastic}_{radiated}$ is the inelastic cross section with the radiative corrections folded in; σ^{D}_{tail}, the calculated radiative tail from the μD elastic scattering peak [21]; σ^{Quasi}_{tail}, the calculated radiative tail from the quasi-elastic peak of μD scatterings; and σ^{P}_{tail}, the calculated radiative tail from elastic μP scatterings. The radiatively corrected cross section at a given (q^2,ν) point was obtained simply by multiplying the measured cross section by the value of δ_R evaluated at that point. The Fermi motion correction was not yet applied, [22] it is less than a few per-

cent in the large ω region we are mainly concerned with. The Glauber correction (nuclear shadowing) is also negligible.

The result on νW_2 per nucleon is shown in Figures 11 through 13, plotted against ω and x respectively. Values of νW_2 were extracted with the assumption of $R = \sigma_L/\sigma_t = 0.18$, and also with R = 0. Since the W_1 term contributed only ~10% in the large ω region, different assumptions of R does not change the result significantly. The range of q^2 values used in Figure 12 is given in Table 1. It is interesting to notice the decrease of νW_2 at large values of ω (or small values of x). There exist numerous theoretical models on the structure functions of deep inelastic scatterings. A few of them in the literature seem to be able to fit this new data without too much trouble. We will briefly mention three interesting ones here.

In a model proposed by Kuti and Weisskopf[23], three valence quarks together with an infinite sea of paired-partons were considered to be confined inside the nucleon. The partons interact among themself through neutral gluons. The interaction of the virtual photon with the valence quarks is assumed to be of the Regge type; and the interaction with the parton sea is of Pomeron type. Their predictions, as shown in Figure 14, appear to be in reasonable agreement with what have been observed.

Another model, suggested by Altarelli, Cabibbo, Maiani, and Petronzio,[24] is quite similar to that of Kuti and Weisskopf. The amusing difference is that each of the constituent quarks, which made up the nucleon, is itself a complex object, made of point-like partons and neutral gluons. The

calculation result, using a complicated $SU(6)_W \otimes O(3)$ theory, also indicated the observed decreasing feature of νW_2 at small values of x as shown in Figure 15.

Other phenomenological models using Regge poles, Pomerons, and fixed poles [25] can all yield the observed shape of νW_2 (see Close and Gunion). The detail can be found in K. Wilson's review. [26]

A very interesting question, which many physicists certainly would like to ask is, "why plot νW_2 at the large ω region where the q^2 values are small?". As shown in Table I, the average q^2 value at $\omega = 200$ is about 1 $(GeV/c)^2$; and at $\omega = 100$, q^2 is about 2 $(GeV/c)^2$. These q^2 values are quite comparable to the well known MIT-SLAC data at $\omega = 20$. The only way to reach higher q^2 values in this large ω region is to do the experiment at muon energies above 150 GeV, and there is plan to do so at Fermilab.

In Figure 16, the plot of νW_2 vs. q^2 is shown for deuterium in the deep inelastic region, $\nu = 90$ to 130 GeV. The rising portion of the plot reflects the decreasing feature of νW_2 as ω increases. The curve does not start to show a sign of leveling off until $q^2 \simeq 3$ $(GeV/c)^2$. It should be noted that for all the new results presented here on νW_2 from Fermilab, no attempt was made to divide the measured quantity by a factor

$$1 - \frac{G_E^2 + \tau G_M^2}{1 + \tau}$$

as it was done in the new electron scattering results from SLAC. [27] In the above expression, G_E and G_M are the elastic nucleon form factors, and $\tau \equiv q^2/4M^2$.

D. Results on Hadron Distributions

The final-state hadrons produced in the high-energy muon scatterings certainly add a new dimension to the study of the deep-inelastic scattering phenomena. It is the hope that the nucleon structure can be understood through the study of the final states. However, as the energy increases, the longitudinal phase volume increases rapidly and the transverse distance only decreases slightly. Therefore it is not very clear what exactly is going to happen. The important handle we have in the muon scattering experiment is the q^2. By comparing various distributions at different ranges of q^2, we may expect to find some clues of the nucleon structure.

The hadrons were measured by the wire chambers immediately before and after the Cyclotron magnet. The muon-electron scattering events were rejected by recognizing that there were only two oppositely-charged coplanar tracks, and that the electron track was characterized by the showers induced in the wire spark chambers behind a 3 r.l. steel radiator. Since there were no further particle identification devices, all the particles were assumed to be pions. The acceptance of each individual hadron was calculated by rotating its momentum vector around that of the virtual photon. Then attempt was made to evaluate the ratio of the hadronic invariant cross-section to the total virtual photoproduction cross section in a specified (q^2,ν) region, which is defined as following:

$$\frac{1}{\sigma_{total}} E_h \frac{d^3\sigma_\gamma}{d\vec{p}^{\,3}} = \frac{1}{\sigma_{total}} \frac{E_h}{\Gamma_t} \frac{d^6\sigma_\mu}{d\vec{p}_h^{\,3}\,(dq^2 d\nu)_\mu}$$

where σ_{total} is the total virtual photoproduction cross section; Γ_t, the virtual photon flux factor. The physical meaning of the above expression is that it represents the probability of producing hadrons in the invariant phase volume $d^3\vec{p}_h/E_h$ per scattered muon. The invariant cross section

$$f \equiv E_h \frac{d^3\sigma_\gamma}{d\vec{P}_h^{\,3}}$$

is averaged over the azimuthal angle. Some of the commonly used single particle, one-dimensional distributions are listed in Table II. From the experimental results, the calculation was done according to the following formula:

$$\frac{1}{\sigma_{total}} E_h \frac{d^3\sigma_\gamma}{d\vec{p}_h^{\,3}} = \frac{\sum^{Hadrons} \left\{ \frac{E_h}{\Gamma_t} \left(\frac{d^6\sigma_\mu}{d\vec{p}_h^{\,3}(dq^2 d\nu)_\mu} \right)^{exp} \delta_R^{Inel}(q^2,\nu) \right\}}{\sum_{\mu'} \left\{ \frac{1}{\Gamma_t} \frac{d^2\sigma}{dq^2 d\nu} \right\}_{\substack{Radiatively \\ corrected}}}$$

where

$$\delta_R^{Inel} = \frac{\sigma^{inel}}{\sigma^{inel}_{radiated}}$$, the inelastic radiative correction factor.

In order to obtain reasonable statistics, the above expression was evaluated over fairly large-sized (q^2,ν) regions to study the q^2-dependence. There is one more complication due to radiative corrections. As shown in Figs. 17(a) and 17(b), the actual 4-momentum transfer is q', instead of the apparent q when there was no radiative corrections. In general, $\vec{q}'$ and $\vec{q}$ are along different directions as indicated in Figure 17(c). In order to calculate the components of hadron momenta with respect to the virtual photon direction correctly, the most probable angle $\theta_{\vec{q}\vec{q}'}$ has to be evaluated first. This was done according a method given by Tsai.[20] We have noticed that in the literatures, the radiative corrections were not applied to most of the hadron electroproduction data. Usually the ratio of the cross sections was simply the ratio of the number of hadrons to the number of scattered muons without any radiative corrections. Part of the results presented here were also done in that manner.

In the following sections, we try to present only a few single hadron inclusive distributions. It is understood that the hadron invariant cross sections had been averaged over the azimuthal angle. The distributions will be displayed over one variable at a time, and the un-used variables will be integrated over the kinematically possible limits as allowed by the specified (q^2,ν) region. All hadrons are assumed to be

pions. At the very recent Erice Summer School, Richard Wilson of the collaboration reported the preliminary results on muo-productions of ρ^o and ρ', F(x') distributions, and total photoabsorption cross sections at 105 and 115 GeV by extrapolation to the limit of $q^2 = 0$.[28] Because of time limitations, I will not try to repeat them at this Symposium. Rather than exhibiting a variety of curves, which may or may not be of relevance, I try to focus on a few salient ones which, I think, are interesting.

1. The $P_\perp^2$-Distribution

The $P_\perp^2$-distributions for hadrons produced in μp scatterings are shown in Figure 18. It is to be noticed that the slope parameter used in the exponential parametrization is smaller for hadrons having large x' values, than those having small x' values.

2. The P_n-Distribution

The component of hadron momentum normal to the muon scattering plane, P_n, is not affected by the radiative corrections because the radiative correction photons are either along the incident or the scattered muon directions. The P_n-distribution is very similar to the "sphericity distribution", which was used in discovering the jets in e^+e^- collisions.[29] Figure 19 shows the P_n-distribution in the deep inelastic region, $\nu = 90$ to 130 GeV, and $q^2 = 1$ to 10 $(\text{GeV/c})^2$. The result indicated that there is no jet structure. The average normal momentum is approximately 250 MeV/c, which is consistent with the $P_\perp^2$-distribution shown before. They should differ by a factor of $\sqrt{2}$.

3. The Missing Mass Spectra and the t-Distributions

The missing mass of a single detected hadron can be easily computed by considering the virtual photon as incident beam. The missing mass spectra for three different (q^2,ν) regions are shown in Figures 20 (a), (b), and (c). The pronounced peak at missing mass value of ~13 GeV, for ν = 90 to 130 GeV, is quite outstanding. To some extent, the shape resembles the effective mass spectrum of (n-1) particles of a n-particle final state ($n \geq 4$), calculated from phase space alone. For lower values of ν (10 to 90 GeV), the ν-dependence of the missing mass spectrum can be seen from Figure 20 (a). In Figure 21, the correlation between $x_{||}$ of the detected pion and its missing mass is shown. The large missing mass is strongly connected with the detected hadrons which have small values of $x_{||}$.

The t-distribution in one of the three different (q^2,ν) regions, corresponding to the missing mass plots, is shown in Figure 22. Since the virtual photons covered a wide range of q^2 and ν, the cross sections are plotted against the difference $|t-t_{min}|$, rather than $|t|$, to adjust for the kinematics differences. Otherwise, the t_{min}-effect of the "broad-band" photon would make the distribution curved when $d\sigma/dt$ is plotted against t. It is to be noted that the t-distributions are exponential and they can be represented by e^{bt}, with $b \simeq 0.8$. By comparing plots in different ranges of q^2, it was observed consistently that the slope parameter b intends to decrease slightly as q^2 increases.

In contrast to a real photon, a virtual photon cannot fragment by itself because of its energy deficiency. As pointed out by Chou and Yang,[30] the virtual photon must absorb first a fraction of the target nucleon before it can materialize into real particles. These "pulverization" products move along the direction of the virtual photon with $x_{\parallel} > 0$. The remaining part of the target nucleon fragments in the usual manner with $x_{\parallel} < 0$. This intuitive picture seems to be in accord with what is shown in Figure 21. However, it is inconclusive. In the present experiment, particles due to target fragmentation completely escaped detection. Actions have been taken to add more detectors to the spectrometer to augment its physics capability in this aspect.

4. The Charge Ratio

The charge ratio, N^+/N^-, for hadrons produced in μP scatterings at 150 GeV is shown in Figure 23. Only in the region of large x', was the q^2-dependence of the charge ratio being seen.

5. The $x_{\parallel}$-Distribution

One of the $x_{\parallel}$-distributions is shown in Figure 24. It was from the data of 150 GeV μD scatterings, and in the deep inelastic region ν = 90 to 130 GeV and q^2 = 1 to 10 $(GeV/c)^2$.

The qualitative conclusion one can draw from the above data is that, in muoproductions at 150 GeV, the inclusive hadron distributions do not show any strong q^2-dependence. Detailed study and comparisons with hadron -hadron collisions will be published by the collaboration shortly.

V. Search for Parity Non-Conservation Effects in Deep-Inelastic μN Interactions

A 20 GeV/c muon experiment had been performed at Serpukhov, U.S.S.R., on the parity-violation effects in deep inelastic μN scatterings.[31]

The experiment was designed to measure the interference between the one-photon exchange amplitude in electromagnetic interactions,

$$4\pi\alpha \langle\mu' | \gamma_\lambda | \mu\rangle \frac{1}{q^2} J_\lambda^{hadron} ,$$

and the neutral current amplitude in weak interactions,

$$\frac{G_o^{(\mu)}}{\sqrt{2}} \langle \mu' | \gamma_\lambda (1+\gamma_5) | \mu \rangle J_\lambda^{hadron} ,$$

where $G_o^{(\mu)}$ is a coupling constant to be measured. The cross section was estimated to be[32]

$$\frac{d^2\sigma}{dq^2 d\nu} = \left(\frac{d^2\sigma}{dq^2 d\nu}\right)_{E.M.} \left\{ 1 + S_\mu \ (3 \text{ to } 4) 10^{-4} \ q^2 \left(\frac{G_o^{(\mu)}}{G_F}\right) \right\}$$

where S_μ is the longitudinal muon polarization; and G_F, the Fermi coupling constant ($10^{-5}/Mp^2$).

The experiment was done by keeping the momentum setting of the negative muon beam line constant at 20 GeV/c. The muon helicity was selected by changing the beam energy of the parent pions from 40 GeV to 28 GeV every 5 accelerator cycles. As shown in Fig. 25, the muon polarization was negative when the muon was selected from the backward decay hemisphere of the pion; and positive, when selected from the forward decay hemisphere. The muon polarization was monitored from time to time by detecting the electrons from muon decay with a shower counter. The experimental apparatus is shown in Fig. 26.

The experimental asymmetry, defined by

$$R = \frac{\sigma(+) - \sigma(-)}{\sigma(+) + \sigma(-)} ,$$

is shown in Fig. 27; where $\sigma(+)$ is the cross section measured with muons of positive helicity; and $\sigma(-)$, cross section measured with muons of negative helicity. This measurement, using 10^{10} muons, gave null result on the asymmetry. And it yielded the following result on the coupling constant

$$G_o^{(\mu)} = (-4 \pm 12)\ G_F$$

Acknowledgements

I wish to express sincere thanks to Drs. Terry Carroll and Leon Rochester, my scientific secretaries, for their invaluable help in preparing this talk and the written version for the proceedings. Thanks are also to Tiana Hunter and Ada Schwartz of the SLAC Publication Office for their generous help in preparing some of the figures.

The results I reported here on the Fermilab E-98 are the fruits of the hard work of my inspiring collaborators from Chicago, Harvard, Illinois and Oxford; and also the joint effort of many members of the Fermilab. I hereby express my admiration to them, in particular R. Fine and R. Heisterberg, for their ceaseless endeavour. Enlightening conversations with Professors Y. Nambu and W.K. Tung are gratefully acknowledged. Finally, I thank Professor R.G. Sachs for his continuing encouragement and help. Also, I owe thanks to the National Science Foundation for their support.

TABLE I

q^2 Range for 150 GeV Deuterium Data

$\langle \omega \rangle$	ω Range	q^2 Range $(GeV/c)^2$	νW_2 (per nucleon)
1.5	1 - 2	11 - 15	0.12
2.5	2 - 3	6 - 15	0.19
3.5	3 - 4	5 - 15	0.24
4.5	4 - 5	4 - 15	0.27
6.0	5 - 7	3 - 15	0.31
8.0	7 - 9	3 - 15	0.33
10.0	9 - 11	3 - 15	0.33
12.5	11 - 14	3 - 15	0.34
17.0	14 - 20	3 - 11	0.34
27.5	20 - 35	3 - 9	0.31
40.0	35 - 45	3 - 6	0.31
52.5	45 - 60	3 - 6	0.31
70.0	60 - 80	2 - 4	0.29
100.0	80 - 120	1.4 - 3	0.25
140.0	120 - 160	1.0 - 2	0.24
200.0	160 - 240	0.8 - 1.4	0.21
320.0	240 - 400	0.6 - 1.0	0.21
500.0	400 - 600	0.3 - 0.5	0.18
800.0	600 - 1000	0.2 - 0.4	0.15

TABLE II

$$f = E \frac{d^3\sigma}{d\vec{p}^3}$$

Notation for f	Variable	Definition
$\frac{d\sigma}{dP_\perp}$	$P_\perp$ (or P_n)	$\frac{E}{\pi} \frac{d\sigma}{2P_\perp dP_\perp}$
$\frac{d\sigma}{dP_\perp^2}$	$P_\perp^2$	$\frac{E}{\pi} \frac{d\sigma}{dP_\perp^2}$
$\frac{d\sigma}{dP_\parallel}$	$P_\parallel$	$\frac{E}{\pi} \frac{d\sigma}{dP_\parallel}$
$\frac{d\sigma}{dX_\parallel}$	$X_\parallel = \frac{P_\parallel^{cm}}{P_{max}^{cm}}$	$\frac{1}{\pi} \frac{E^{cm}}{P_{max}^{cm}} \frac{d\sigma}{dX_\parallel}$
$\frac{d\sigma}{dX_\perp}$	$X_\perp = \frac{P_\perp}{P^{cm}}$	$\frac{1}{\pi} \frac{E}{2P_\perp P_{max}^{cm}} \frac{d\sigma}{dX_\perp}$
$\frac{d\sigma}{dy}$	$y = \frac{1}{2} \ln\left(\frac{E + P_\parallel}{E - P_\parallel}\right)$	$\frac{1}{\pi} \frac{d\sigma}{dy}$
$\frac{d\sigma}{d\xi}$	$\xi = \frac{y - y_{target}}{y_{max} - y_{target}}$	$\frac{1}{\pi(y_{max} - y_{target})} \frac{d\sigma}{d\xi}$
$\frac{d\sigma}{d(MM)}$	MM	$\frac{1}{\pi} \sqrt{\Delta(S,-q^2,M^2)} \frac{d\sigma}{2(MM)d(MM)}$
$\frac{d\sigma}{dt}$	t	$\frac{1}{\pi} \sqrt{\Delta(S,-q^2,M^2)} \frac{d\sigma}{dt}$

APPENDIX

KINEMATICS OF DEEP INELASTIC MUON SCATTERING

Variables:

E_o = Energy of incident muon (lab)

P_o = Momentum of incident muon (lab)

E' = Energy of scattered muon (lab)

P' = Momentum of scattered muon (lab)

θ = Angle of scattered muon (lab)

ν = Energy loss of scattered muon (lab)

q^2 = 4-momentum transfer squared ($q^2 \geq 0$)

W = Total mass of final hadron system

$S = W^2$

$\omega = \frac{2M\nu}{q^2}$ (Bjorken scaling variable)

$x = \frac{1}{\omega}$ (Feynman scaling variable)

MM = missing mass of single pion in virtual photoproduction

t = momentum transfer squared when single hadron is detected in virtual photoproduction

$P_{||}$ = hadron momentum along the direction of virtual photon

$P_{\perp}$ = hadron momentum perpendicular to the direction of virtual photon

M = proton (neutron) mass

m_μ = muon mass

m_π = pion mass

Formulae:

$$q^2 = 2\,(E_o E' - P_o P' \cos\theta - m_\mu^2)$$

$$W^2 = 2M\nu + M^2 - q^2$$

$$\nu = E_o - E'$$

$$MM^2 = W^2 + m_\pi^2 - 2E_\pi\,(\nu + M) + 2P_{||}\,\sqrt{q^2 + \nu^2}$$

$$t = -q^2 + m_\pi^2 - 2E_\pi \nu + 2P_\parallel \sqrt{q^2 + \nu^2}$$

$$t_{min} = -q^2 + m_\pi^2 - 2E_\pi \nu + 2P_\pi \sqrt{q^2 + \nu^2}$$

$$P_{max}^{CM} = \frac{\sqrt{\Delta(W^2, m_\pi, (M + m_\pi)^2)}}{2W}$$

$$\Delta(x,y,z) = x^2 + y^2 + z^2 - 2xy - 2yz - 2zx$$

<u>Cross Section and Structure Functions:</u>

$$\frac{d^2\sigma}{d\Omega dE'} = \frac{2\alpha^2}{q^4} \left(\frac{P'}{E_o}\right) \left[\left(2 E_o E' - \frac{q^2}{2}\right) W_2 (q^2, \nu) + (q^2 - 2m_\mu^2) W_1 (q^2, \nu) \right]$$

$$\frac{d^2\sigma}{dq^2 d\nu} = \left(\frac{\pi}{E_o E'}\right) \frac{d^2\sigma}{d\Omega dE'}$$

$$\frac{d^2\sigma}{dq^2 d\nu} = \Gamma_t (\sigma_t + \varepsilon\sigma_L) = \Gamma_t \sigma_{total}$$

$$\Gamma_t = \frac{\alpha}{2\pi^2} \left(\frac{K}{q^2}\right) \left(\frac{E'}{E_o}\right) \frac{1}{(1 - \varepsilon)} \left(\frac{\pi}{E_o E'}\right)$$

$$K = \frac{W^2 - M^2}{2M}$$

$$\varepsilon = \frac{1}{1 + \dfrac{2(q^2 + \nu^2) \tan^2 \theta/2}{q^2 (1 - q_{min}^2 / q^2)^2}}$$

$$q_{min}^2 = 2 (E_o E' - P_o P' - m_\mu^2)$$

$$W_1 = \frac{K}{4\pi^2 \alpha} \sigma_t$$

$$W_2 = \frac{K}{4\pi^2 \alpha} \frac{q^2}{q^2 + \nu^2} (\sigma_t + \sigma_L)$$

$$\frac{W_1}{W_2} = \left(1 + \frac{\nu^2}{q^2}\right) \frac{1}{1 + R}$$

$$R = \sigma_L/\sigma_t$$

<u>Bjorken Scaling Function ($\nu \to \infty$, $q^2 \to \infty$, ω finite)</u>:

$$2M\, W_1(\nu, q^2) \to F_1(\omega)$$

$$\nu W_2\ (\nu, q^2) \to F_2\ (\omega)$$

References and Footnotes

(1) W.K.H. Panofsky, C.M. Newton, and G.B. Yodh, Phys. Rev. 98, 751(1955); W.K.H. Panofsky, W.M. Woodward and G.B. Yodh, Phys. Rev. 102, 1392(1956).

(2) W.K.H. Panofsky and E.A. Allton, Phys, Rev. 110, 1155(1958).

(3) R.H. Dalitz and D.R. Yennie, Phys. Rev. 105, 1598(1957).

(4) S. Fubini, Y. Nambu, and V. Wataghin, Phys. Rev. 111, 329(1958).

(5) W.K.H. Panofsky, Proceedings of 14th International Conference on High Energy Physics, Viena, Austria, 1968, J. Prentki and J. Steinberger, editors, p.23.

(6) M. Breidenbach, J.I. Friedman, and H.W. Kendall; and E.D. Bloom, D.H. Coward, H. DeStaebler, J. Drees, L.W. Mo, and R.E. Taylor, Phys. Rev. Letters 23, 935(1969).

(7) F.W. Brasse, Proceedings of the 6th International Symposium on Electron and Photon Interactions at High Energies, Bonn, Germany, 1973, H. Rollnik and W. Pfeil, editors, p.251, North-Holland Publishing Co., Amsterdam.
F.J. Gilman, Proceedings of the 17th International Conference on High Energy Physics, London, 1974, J.R. Smith, editor, p.IV-149, Rutherford Laboratory, Chilton, Didcot, U.K.

(8) R.P. Feynman, p.237.
C.N. Yang, p.509.
High Energy Collisons, 3rd International Conference, Stony Brook, 1969, C.N. Yang, J.A. Cole, M. Good, R. Hwa, J. Lee-Franzini, organizers.

(9) Y. Watanabe, L.N. Hand, S. Herb, and A. Russell; and C. Chang, K.W. Chen, D.J. Fox, A. Kotlewski, and P.F. Kunz; and S.C. Loken, and M. Strovink; and W. Vernon, contributed paper to the Symposium No. 118; and also No. 119.

(10) L.N. Hand, Phys. Rev. 129, 1834(1963). Also, S.M. Berman, Phys. Rev. 135, 1249(1964).

(11) Wu-ki Tung, Preprint EFI 75/14, University of Chicago, 1975; also contributed paper to the Symposium No. 171.

(12) V.N. Gribov, Soviet Phys. JETP 30, 709(1970).

(13) J.J. Sakurai and I. Schildknecht, Phys. Letters 40B, 121(1972).

(14) H.T. Nieh, Phys. Letters 53B, 344(1974).

(15) M.S. Chanowitz and S.D. Drell, Phys. Rev. Letters 30, 807(1973); Phys. Rev. D9, 2078(1974).

(16) B. Richter, Proceedings of the 17th International Conference on High Energy Physics, London, 1974, J.R. Smith, editor, p.IV-37, Rutherford Laboratory, Chilton, Didcot, U.K.

(17) The following people are presently engaged in the muon scattering program: H.L. Anderson, V.K. Bharadwaj. N.E. Booth, W.R. Francis, R.M. Fine, B.A. Gordon, R.H. Heisterberg, R.G. Hicks, G.I. Kirkbride, T.B.W. Kirk, W.A. Loomis, H.S. Matis, L.W. Mo, L.C. Myrianthopoulos, F.M. Pipkin, S.H. Pordes, T.W. Quirk, W.D. Shambroom, A. Skuja, L.J. Verhey, W.S.C. Williams, Richard Wilson and S.C. Wright.

(18) Anderson, Fermi, Long, Martin, and Nagle, Phys. Rev. 85, 934(1952)
Anderson, Fermi, Long and Nagle, Phys. Rev. 85, 936(1952).
K.A. Brueckner, Phys. Rev. 86, 106(1952).
I wish to thank Professor Robert R. Wilson for telling me the significance of Brueckner's analysis, which I was ignorant, immediately after my talk at this Symposium.

(19) L.W. Mo and Y.S. Tsai, Rev. Mod. Phys. 41, 205(1969).

(20) Y.S. Tasi, "Radiative Corrections to Electron Scattering", Report No. SLAC-PUB-848, Stanford Linear Accelerator Center (1971).

(21) Y.S. Tsai, Proceedings of the International Conference on Nuclear Structure, 1963 (Stanford University Press, Stanford, California, 1964) p.221. The elastic form factors of deuteron used was that defined by T.A. Griffy and L.I. Schiff, High Energy Physics, Vol. I, p.341, E.H.S. Burhop, editor, Academic Press, N.Y. 1967. The deuteron wave function used was that given by R.V. Reed, Jr., Ann. Phys. 50, 411(1968).

(22) W.B. Atwood and G.B. West, Phys. Rev. D7, 773(1973).

(23) J. Kuti and V.F. Weisskopf Phys. Rev. D4, 3418(1971).
The modified Kuti-Weisskopf model was given by R. McElhaney and S.F. Tuan, Phys. Rev. D7, 2267(1963), and also Nucl. Phys. B72, 487(1974).

(24) G. Altarelli, N. Cabibbo, L. Maiani and R. Petronzio, CERN Report Ref. TH.1727-CERN, 1973; also Nucl. Phys. B69, 531(1974).

(25) Fixed pole for νW_2 was proposed by T.P. Cheng and W.K. Tung, Phys. Rev. Letters 24, 851(1970). Calculation of νW_2 was done by F.E. Close and J.F. Gunion, Phys. Rev. D4, 742(1971). A review was given by F.J. Gilman, SLAC Report No. SLAC-167, Vol. I, p.82 (Proceedings of SLAC Summer Institute on Particle Physics, 1973).

(26) K. Wilson, Proceedings of the 1971 International Symposium on Electron and Photon Interactions at High Energies, Cornell University, Ithaca, N.Y., 1971, N.B. Mistry, M.E. Nordberg, Jr., and G. Grammer, Jr., editors, p.116.

(27) S. Stein, W.B. Atwood, E.D. Bloom, R.L.A. Cottrell, H.DeStaebler, C.L. Jordan, H.G. Piel, C.Y. Prescott, and R.E. Taylor, SLAC-PUB-1528, 1975. Submitted to Phys. Rev.

(28) Richard Wilson, "Scattering of Muons at 150 GeV", Proceedings of the Erice Summer School, Erice, Italy, 1975.

(29) R. Schwitters, Invited talk at this Symposium.

(30) T.T. Chou and C.N. Yang, Phys. Rev. D4, 2005(1971).

(31) Yu. B. Bushnin, A.F. Dunaytzev, R.I. Dzhelyadin, S.V. Golovkin, V.F. Konstantinov, V.P. Kubarovsky, L.G. Landsberg, V.M. Leontyev, G.P. Makarov, V.A. Mukhin, A.N. Prokhorov, V.G. Rybakov, V.A. Senko, Yu.N. Simonov, V.V. Smirnov, V.P. Sugonyaev, A. Zallo, A.M. Zaytzev, contributed paper to this Symposium.

(32) Ya.B. Zeldovich and A.M. Perelomov, Soviet Physics JETP 12, 777(1961), A. Love, G.G. Ross, and D.V. Nanopoulos, Nucl. Phys. B49, 513(1972); R.Petronzio, Roma Preprint No. 411, 1973 (unpublished); E. Derman, Phys. Rev. D7, 2755(1973); N.N. Nikolaev, M.A. Shifman, and M.Zh. Shmatikov, ZhETF Pisma 18, 70(1973), and also Soviet Physics JETP Letters 18, 39(1973); C.H. Llewellyn-Smith, Proceedings of the Conference on e^+e^- and ep Storage Rings, DESY 73/66, p.95; M. Suzuki, Nucl. Phys. B70, 154(1974); S.M. Berman and J.R. Primack, Phys. Rev. D9, 2171(1974); W.J. Wilson, "Parity violation in deep-inelastic charged lepton-hadron scattering", Harvard preprint (1974); C.P. Korthals-Altes, M. Perrottet, and E. de Rafael, Nucl. Phys. B76, 549(1974); C.H. Llewellyn-Smith, CERN Report TH.1710-CERN (1973); C.H. Llewellyn-Smith, and D.V. Nanopoulos, Nucl. Phys. B78, 205(1974), erratum on this paper can be found in Nucl. Phys. B83, 544(1974).

Figure Captions

Figure 1 Isometric plot of the inelastic electron scattering cross sections vs. q^2 and final state mass [Panofsky and Allton, Phys. Rev. 110, 1155(1958)].

Figure 2 Schematic layout of the muon beam at Fermilab. This beam was designed by T. Yamanouchi.

Figure 3 Schematic of the muon beam optics at Fermilab.

Figure 4 The experimental apparatus used in the test of Bjorken scaling at Fermilab by the Cornell-Michigan State - LBL - La Jolla collaboration. Shown are the configurations for experimentation with 150 GeV (top) and 56 GeV (bottom) incident muons.

Figure 5 The kinematical region explored by the test of Bjorken scaling experiment at Fermilab.

Figure 6 The experimental result of $r(\omega,q^2)$. Solid lines are power-law fits to data, drawn through all data and also bands of $v = q^2/2ME$. The effect of changing the spectrometer calibration by 1% is indicated by the dashed line. df is the abbreviation of degrees of freedom.

Figure 7 Ratio of observed to "Monte Carloed" event rate vs. q^2 for eight ranges of ω.

Figure 8 The schematic layout of the muon-nucleon scattering spectrometer at Fermilab. This spectrometer was built by a Chicago-Harvard-Illinois-Oxford collaboration.

Figure 9 A typical reconstructed muon scattering event. The data is from 150 GeV μ^+ on a liquid deuterium target. The dotted vertical lines indicate the scintillation counters which fired.

Figure 10 The kinematical region explored by the Chicago-Harvard-Illinois-Oxford $\mu P/\mu D$ scattering experiment. In the shaded area, there were a number of counts of low statistics which were not included in the results presented at this Symposium.

Figure 11 νW_2 of proton vs. $\omega = 2M\nu/q^2$. The solid curve is the recent SLAC electron scattering result[27].

Figure 12 νW_2 of deuteron divided by 2 vs. ω. The triangles are calculated from the recent SLAC result.[27]

Figure 13 νW_2 of deuteron divided by 2 vs. $x = q^2/2M\nu$. In this plot, all data points have $q^2 \gtrsim 1\ (\mathrm{GeV}/c)^2$.

Figure 14 Kuti-Weisskopf's model on νW_2 vs. $x' = q^2/(q^2+W^2)$. Dashed line is the best fit to SLAC data points using $g = 1$. The dash-dot-dot-dot line is the sea contribution.

Figure 15 νW_2 by the model of Altarelli, Cabibbo, Maiani, and Petronzio. The data points are from SLAC. The solid line represents the full structure function. The dashed line corresponds to omitting the $q\bar{q}$ pair contributions.

Figure 16 νW_2 for deuteron divided by 2 vs. q^2 in the deep inelastic region $\nu = 90$ to 130 GeV.

Figure 17 (a) When there is radiative corrections, the 4-momentum of virtual photon, q', is determined by the unkown quantities, E_s' and E_p'. E_s is the incident muon, and E_p the scattered muon energy.

(b) When there is no radiative corrections, the 4-momentum of the virtual photon, q, is uniquely determined by the momenta of the incident and the scattered muon.

(c) The relationship between $\vec{q}$ and $\vec{q}'$. The scattering plane is the xz-plane. In the framework of peaking approximations, $\vec{q}'$ stays in the xz-plane.

Figure 18 $P_\perp^2$-distributions for pions produced in μP scatterings. x' is defined as $x' \equiv P_{\parallel}^{cm}/(P_{max}^{cm\,2} - P_\perp^{\,2})^{1/2}$. Radiative corrections was not included in this plot.

Figure 19 P_n-distribution of muo-produced pions from deuterium at 150 GeV. P_n is the component of hadron momentum perpendicular to the muon scattering plane. The plot is for data in the deep inelastic region ν = 90 to 130 GeV and q^2 = 1 to 10 $(GeV/c)^2$.

Figure 20 Missing mass spectra of a single detected pion in virtual photoproductions.

(a) ν = 10 to 90 GeV, q^2 = 3 to 15 $(GeV/c)^2$.

(b) ν = 90 to 130 GeV, q^2 = 0.3 to 1.0 $(GeV/c)^2$.

(c) ν = 90 to 130 GeV, q^2 = 1 to 10 $(GeV/c)^2$.

Figure 21 The correlation between $x_{\parallel}$ of the detected single hadron and its missing mass in virtual photoproductions for ν = 90 to 130 GeV, and q^2 = 0.3 to 1.0 $(GeV/c)^2$. The lengths of the slashes indicate the relative population.

Figure 22 The t-distributions in virtual photoproductions for ν = 90 to 130 GeV, and q^2 = 1 to 10 $(GeV/c)^2$; where t is the squared 4-momentum difference between the incident virtual photon and the detected pion, t_{min} is the value of t when the detected pion is along the direction of the virtual photon.

Figure 23 The charge ratio, N^+/N^-, of hadrons produced in 150 GeV μP scatterings.

Figure 24 $x_{\parallel}$-distribution of hadrons produced in 150 GeV μD scatterings. The (q^2,ν) range is ν = 90 to 130 GeV, and q^2 = 1 to 10 $(GeV/c)^2$.

Figure 25 Principle of producing muon beams with different longitudinal polarizations. S_μ is the muon polarization. (a) $E_\mu \simeq 20$ GeV, $E_\pi^{(1)} \simeq 40$ GeV. (b) $E_\mu \simeq 20$ GeV, $E_\pi^{(2)} \simeq 28$ GeV.

Figure 26 Experimental apparatus for search for parity violation effects in deep inelastic μN interactions at Serpukhov. T is a steel-calorimeter target assembly; H_4, H_5, H_6 are scattered muon detectors.

Figure 27 Experimental results on the asymmetry R vs. q^2 for different incident muon energies. λ is the difference in longitudinal polarizations for muons of opposite helicities.

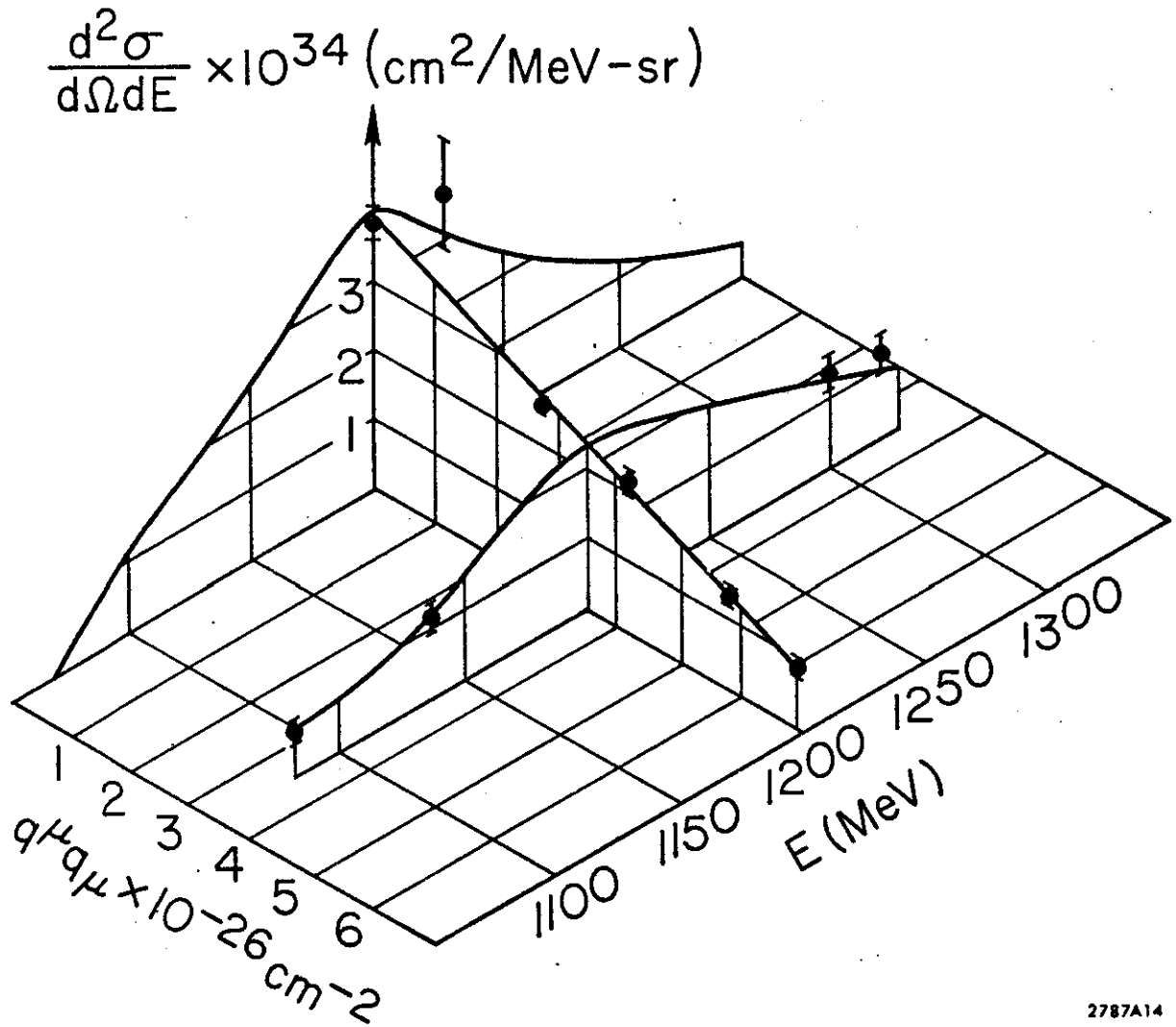
$\frac{d^2\sigma}{d\Omega dE} \times 10^{34}$ (cm²/MeV-sr)
3
2
1
1
2
3
4
5
6
$q^\mu q_\mu \times 10^{-26}$ cm^{-2}
1100
1150
1200
1250
1300
E (MeV)
2787A14

FIG. 1

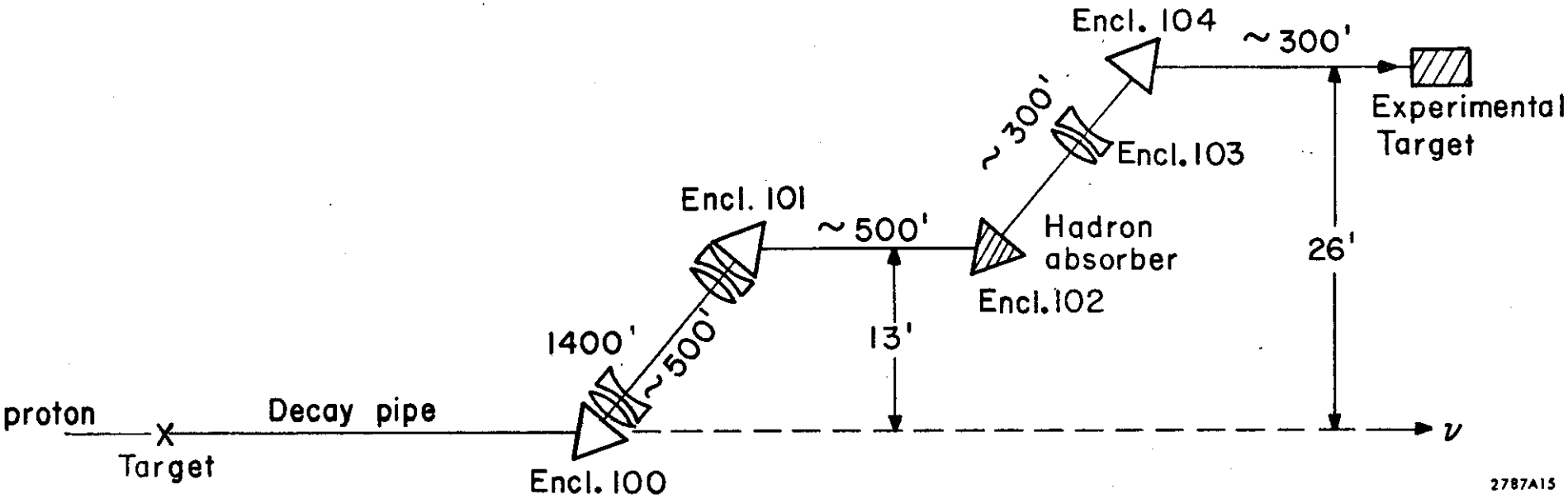
Encl. 104
~ 300'
Experimental
Target
~ 300'
Encl. 103
Encl. 101
~ 500'
Hadron
absorber
26'
Encl. 102
1400'
~ 500'
13'
proton
Decay pipe
ν
Target
Encl. 100
2787A15

FIG. 2

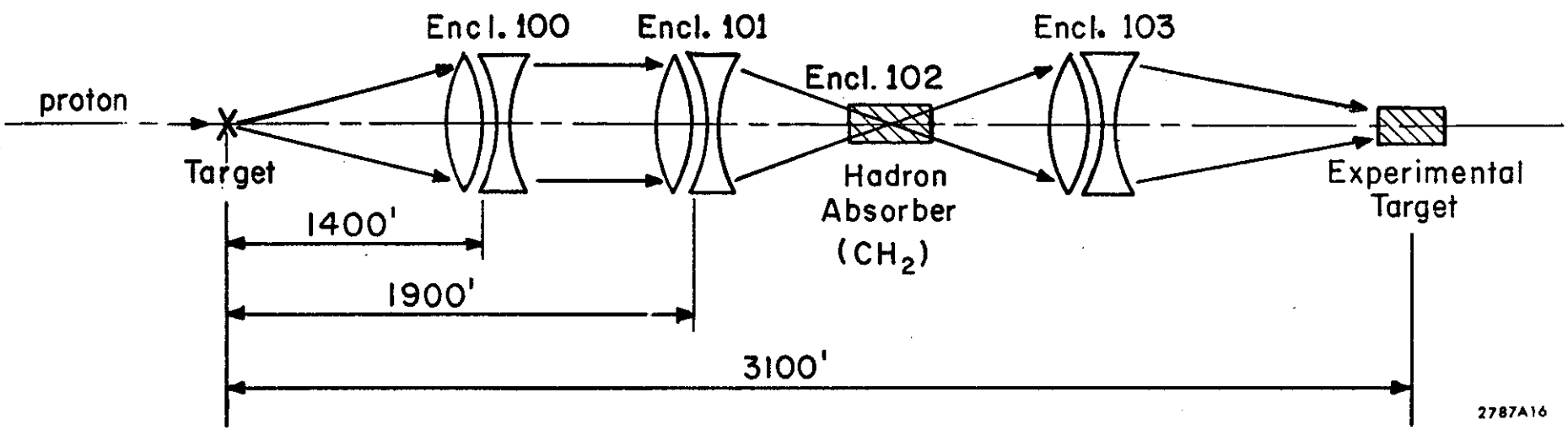
proton
Target
Encl. 100
Encl. 101
Encl. 102
Encl. 103
Hadron
Absorber
(CH_2)
Experimental
Target
1400'
1900'
3100'
2787A16

FIG. 3

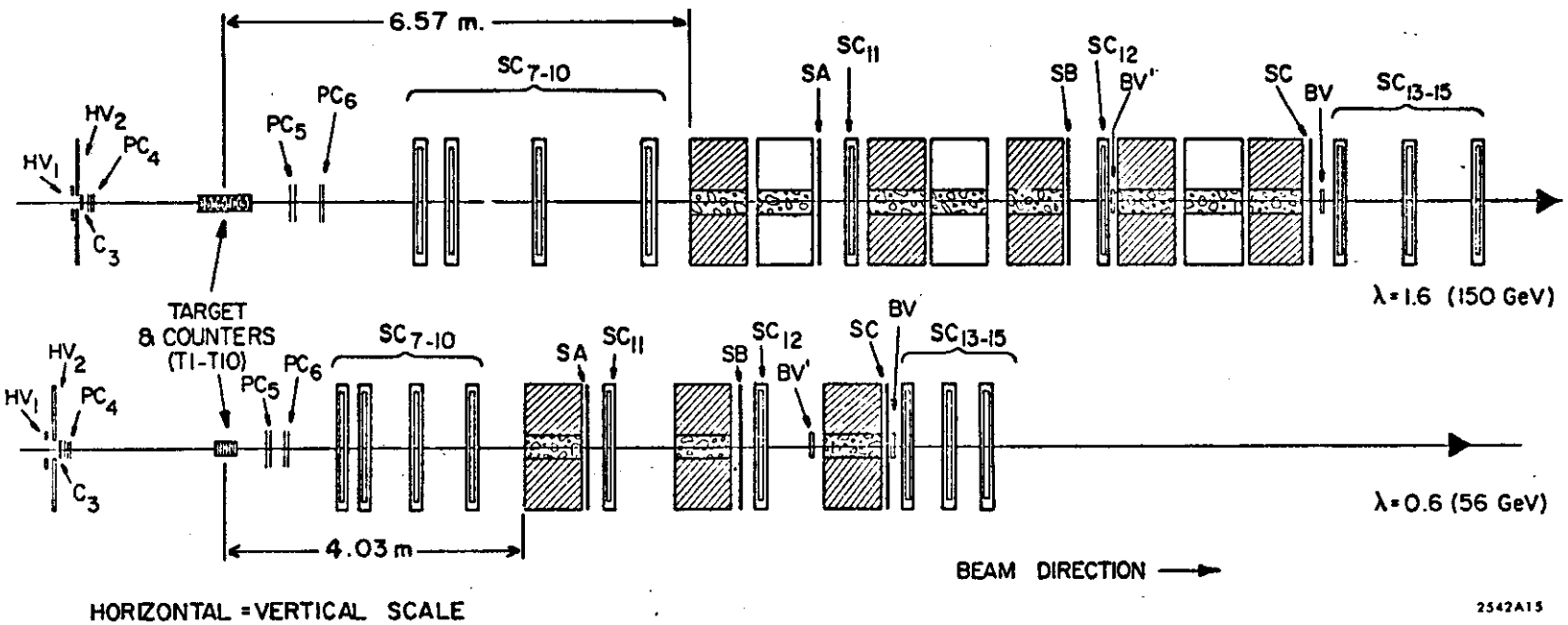
6.57 m.
HV1
HV2
PC4
C3
TARGET
& COUNTERS
(T1-T10)
PC5
PC6
SC7-10
SA
SC11
SB
SC12
BV'
SC
BV
SC13-15
λ = 1.6 (150 GeV)
λ = 0.6 (56 GeV)
4.03 m
BEAM DIRECTION
HORIZONTAL = VERTICAL SCALE
2542A15

FIG. 4

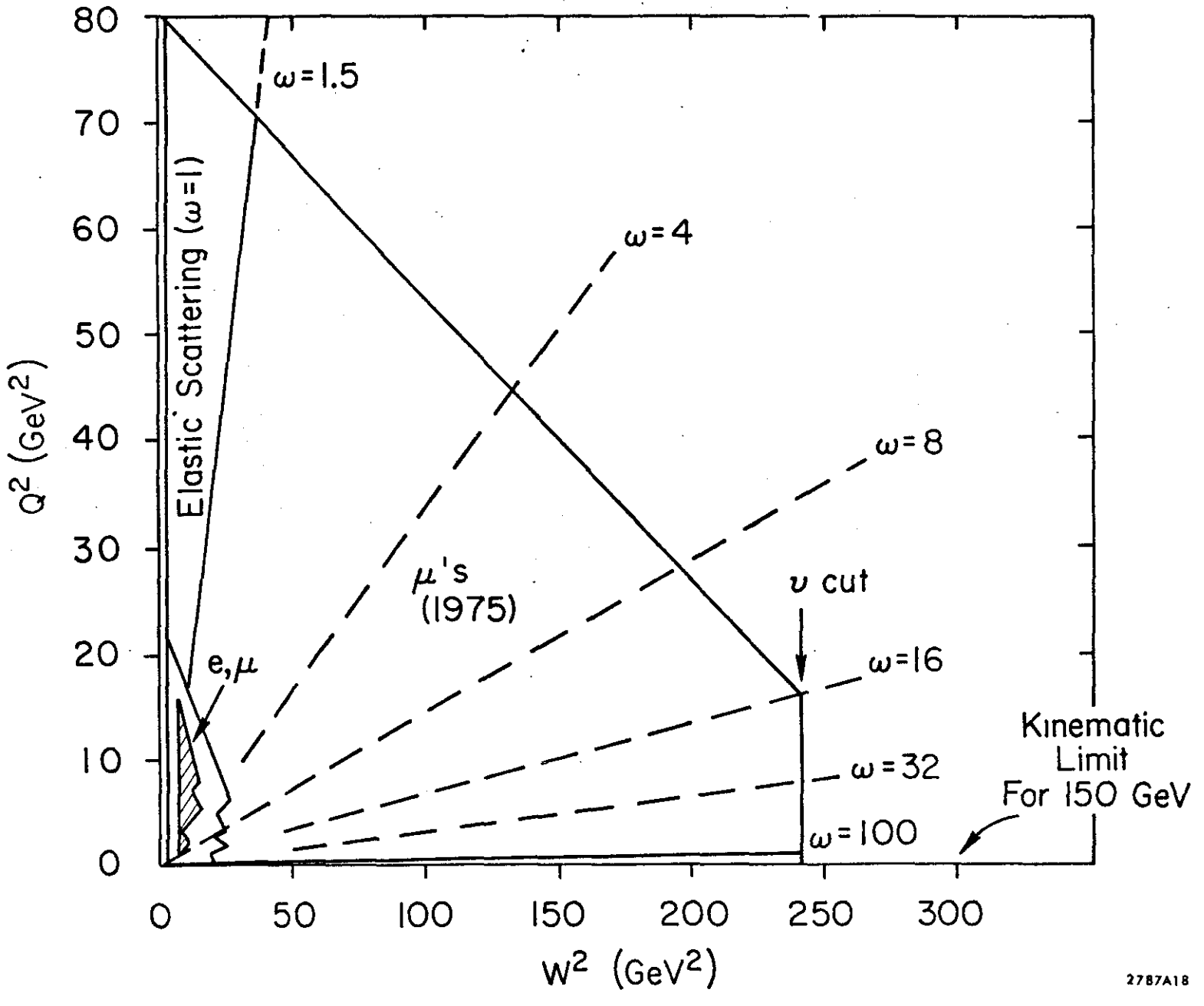
80
70
60
50
40
30
20
10
0
Q^2 (GeV^2)
0
50
100
150
200
250
300
W^2 (GeV^2)
Elastic Scattering (ω=1)
ω=1.5
ω=4
ω=8
ω=16
ω=32
ω=100
μ's
(1975)
e,μ
ν cut
Kinematic
Limit
For 150 GeV
2787A18

FIG. 5

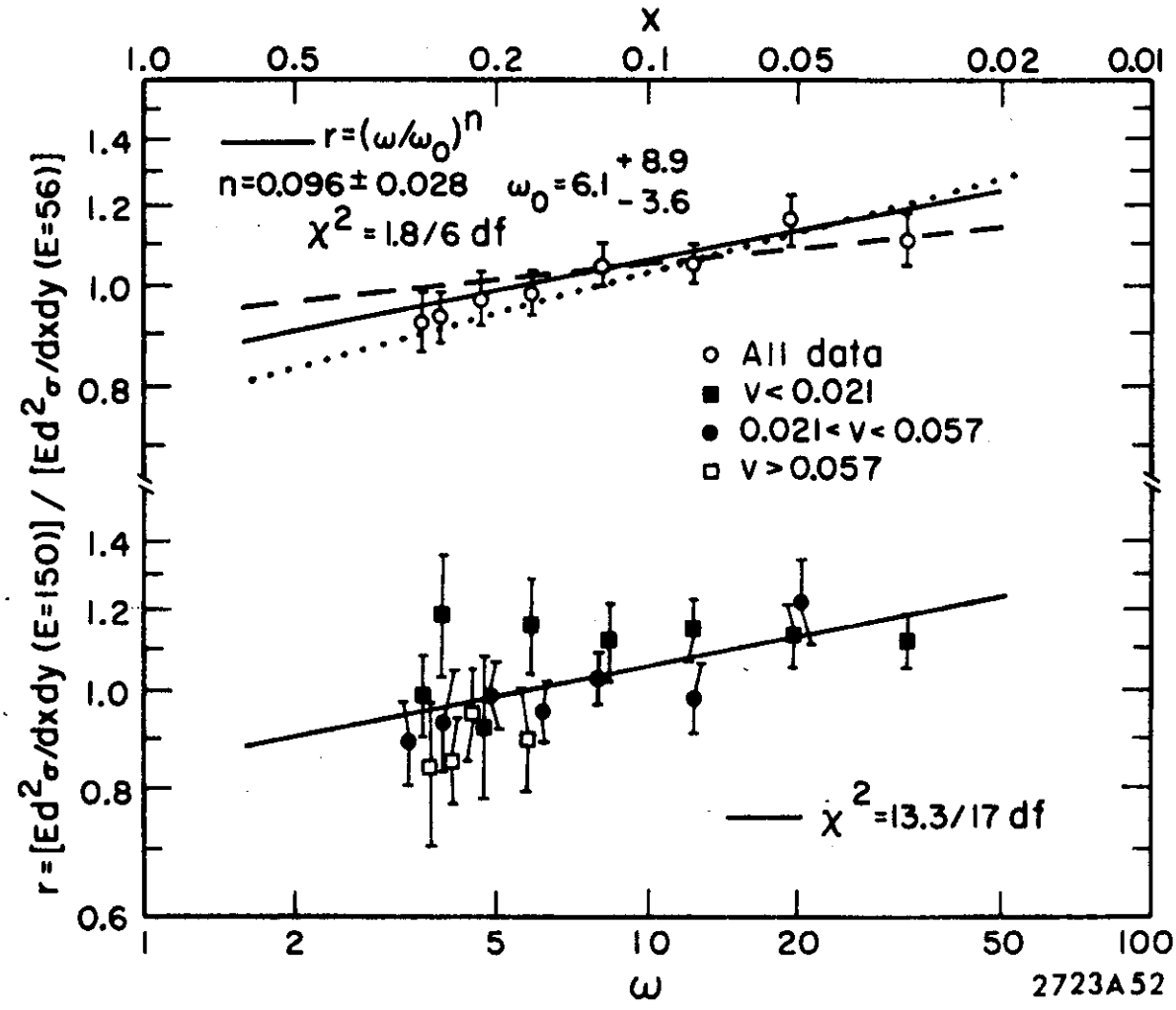
x
1.0
0.5
0.2
0.1
0.05
0.02
0.01
r=(ω/ω0)^n
n=0.096 ± 0.028
ω0=6.1 +8.9 -3.6
χ2 = 1.8/6 df
All data
v< 0.021
0.021< v< 0.057
v > 0.057
χ2=13.3/17 df
r = [Ed2σ/dxdy (E=150)] / [Ed2σ/dxdy (E=56)]
1.4
1.2
1.0
0.8
0.6
1
2
5
10
20
50
100
ω
2723A52

FIG. 6

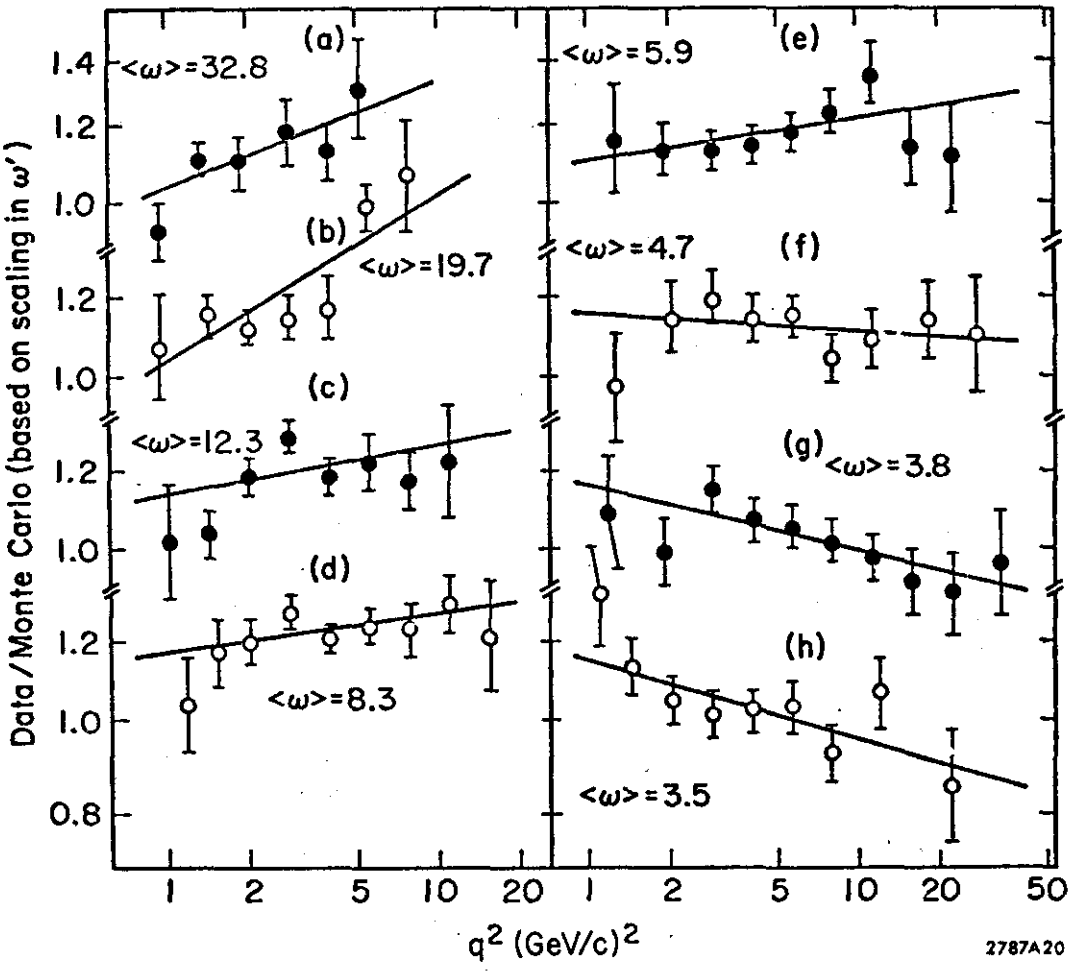
(a)
<ω>=32.8
(b)
<ω>=19.7
(c)
<ω>=12.3
(d)
<ω>=8.3
(e)
<ω>=5.9
(f)
<ω>=4.7
(g)
<ω>=3.8
(h)
<ω>=3.5
Data/Monte Carlo (based on scaling in ω')
q² (GeV/c)²
2787A20

FIG. 7

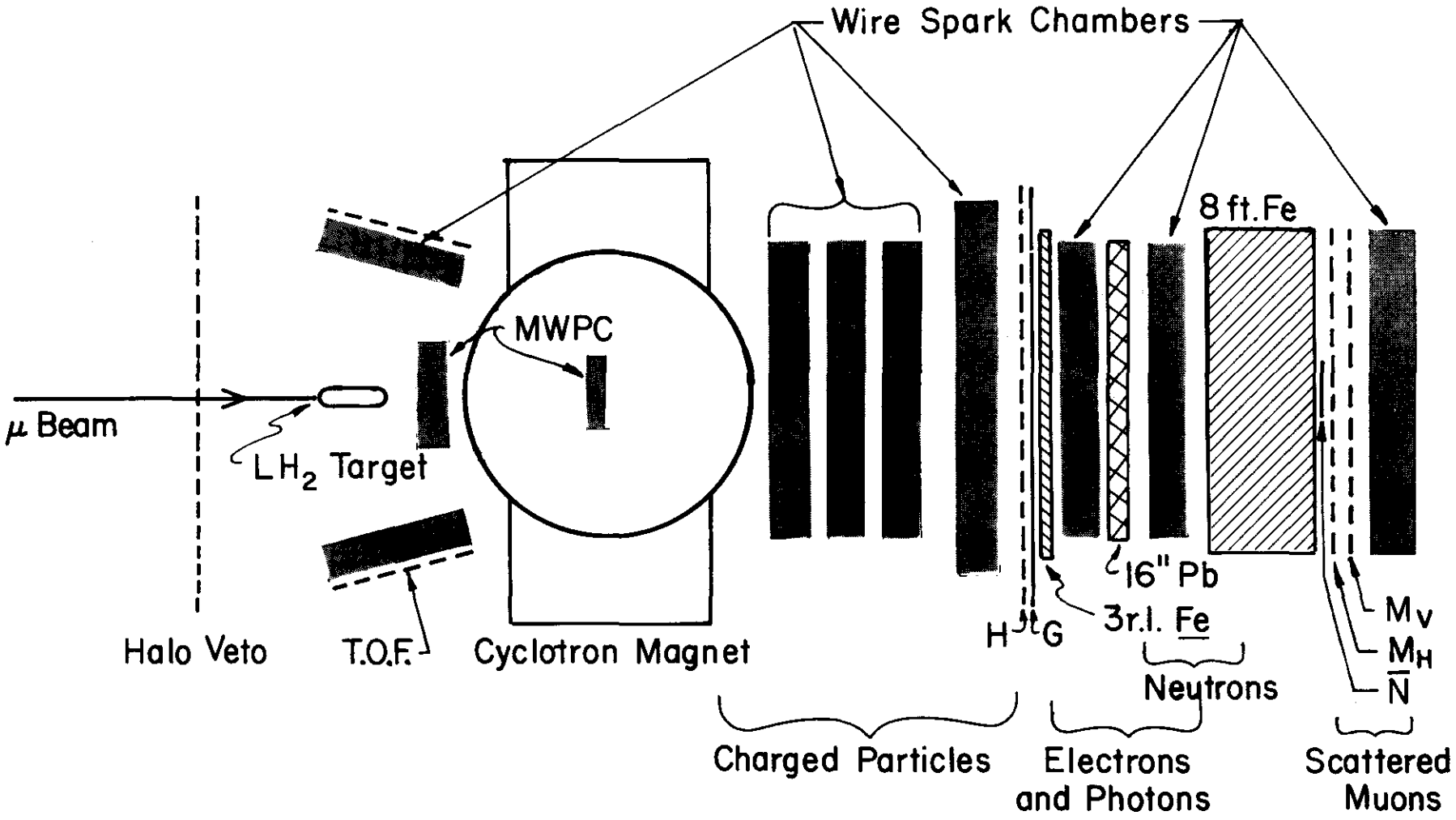
Wire Spark Chambers
8 ft. Fe
MWPC
μ Beam
LH2 Target
Halo Veto
T.O.F.
Cyclotron Magnet
H
G
16" Pb
3r.l. Fe
Neutrons
Mv
MH
N̄
Charged Particles
Electrons and Photons
Scattered Muons

FIG. 8

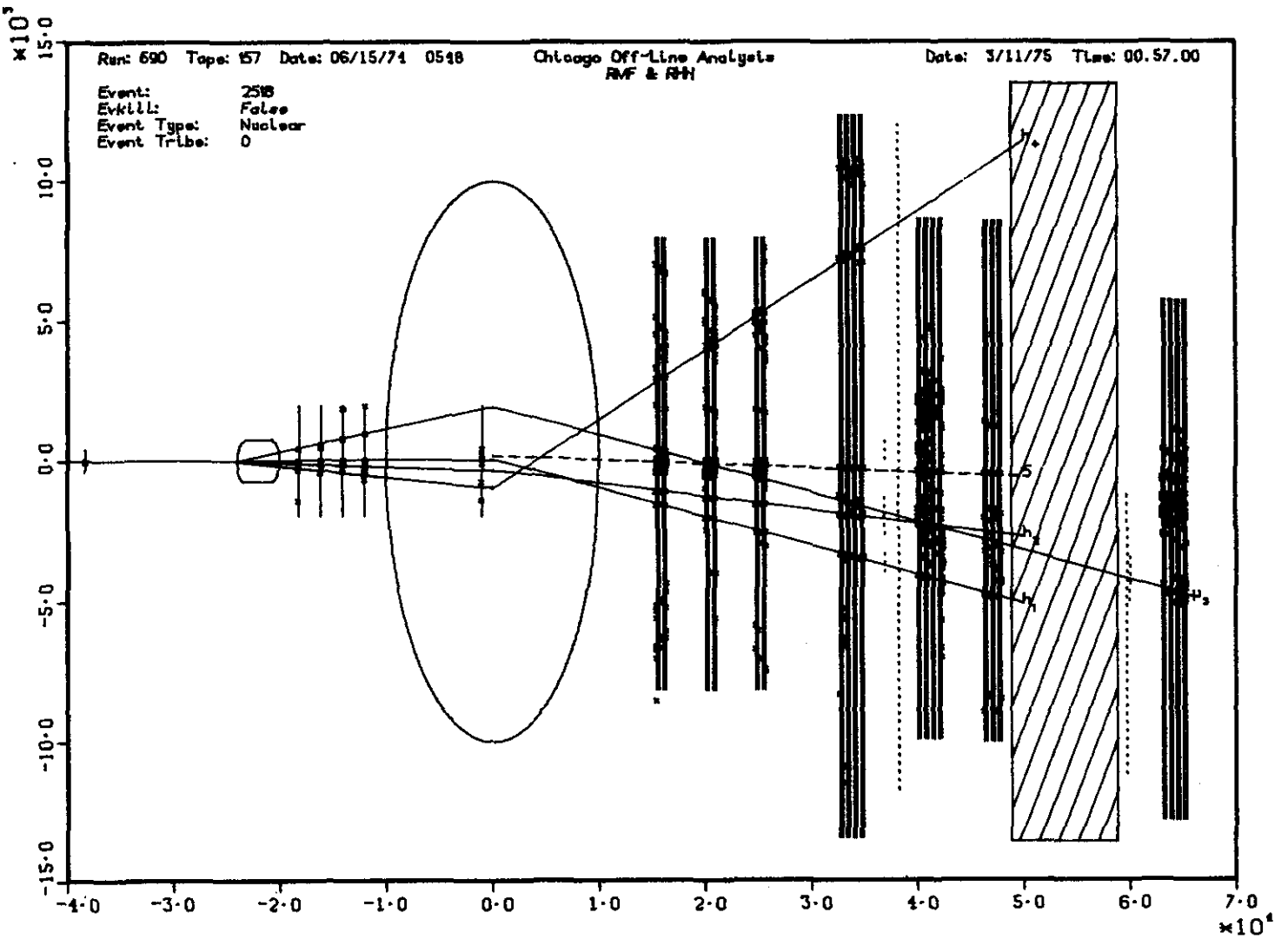
Run: 690 Tape: 157 Date: 06/15/71 0548
Chicago Off-Line Analysis
RMF & RHH
Date: 3/11/75 Time: 00.57.00
Event: 2518
Evkill: False
Event Type: Nuclear
Event Tribe: 0
×10³
15·0
10·0
5·0
0·0
-5·0
-10·0
-15·0
-4·0
-3·0
-2·0
-1·0
0·0
1·0
2·0
3·0
4·0
5·0
6·0
7·0
×10⁴

FIG. 9

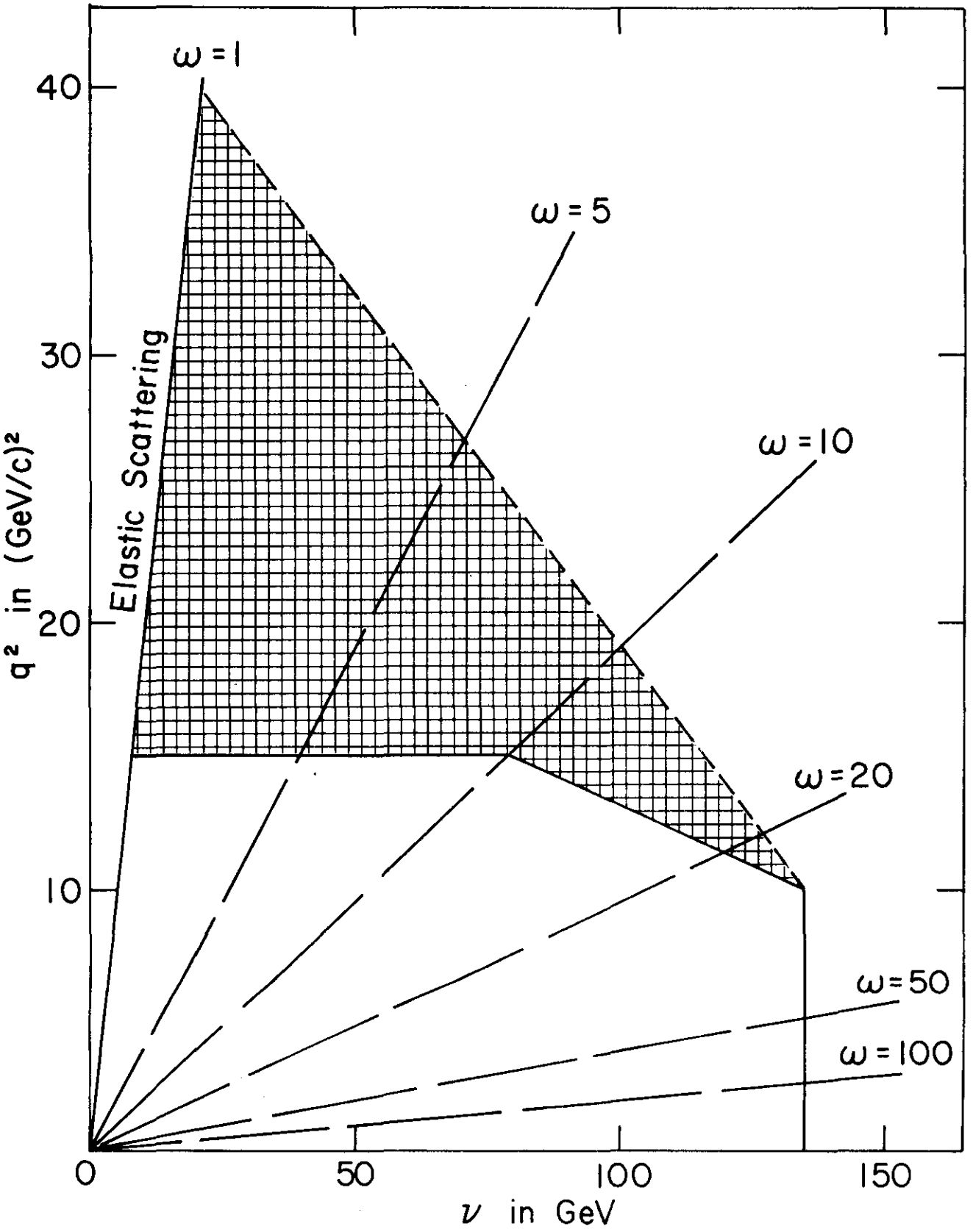
ω = 1
ω = 5
ω = 10
ω = 20
ω = 50
ω = 100
Elastic Scattering
40
30
20
10
0
50
100
150
q² in (GeV/c)²
ν in GeV

FIG. 10

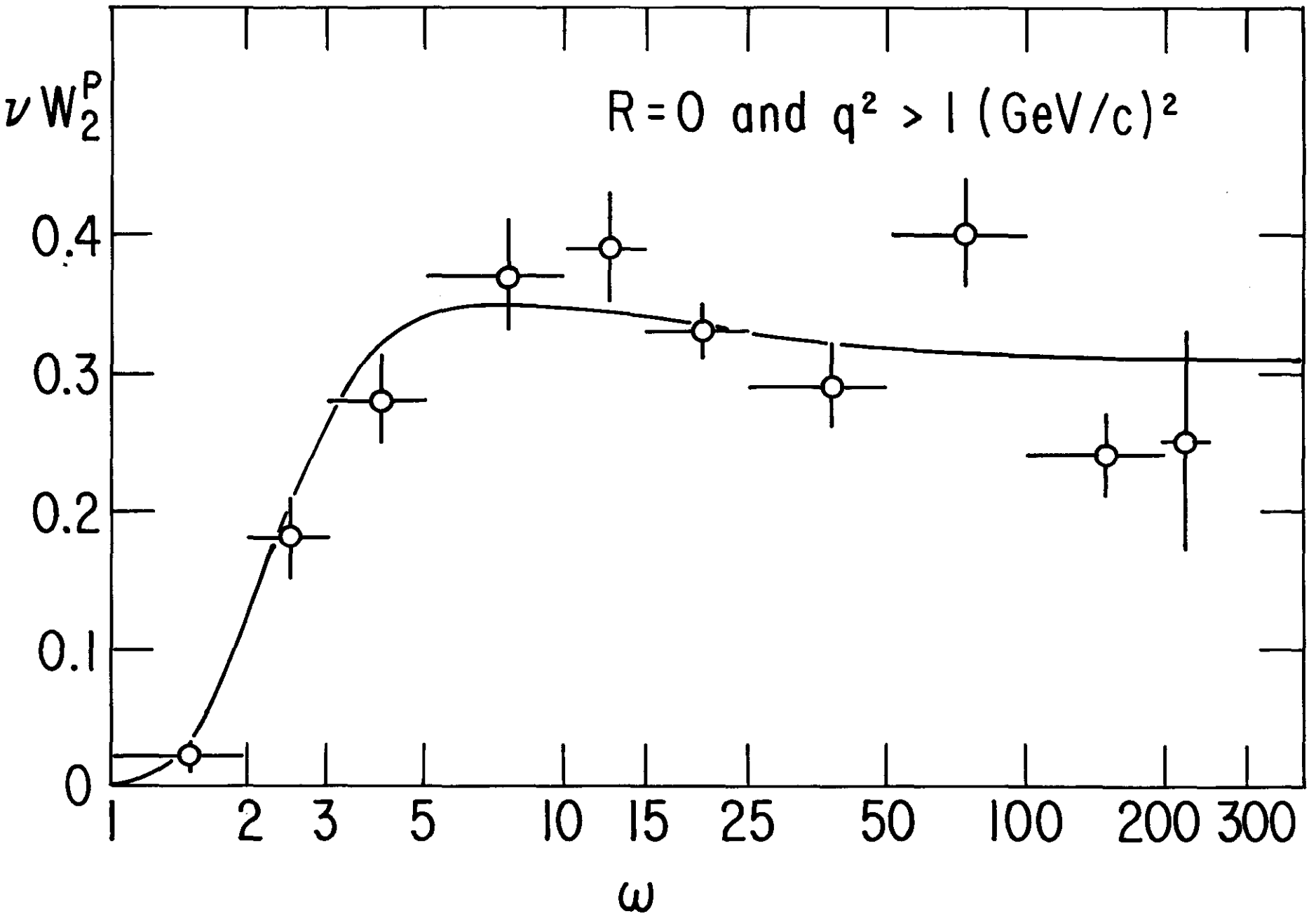
νW_2^p
R = 0 and $q^2 > 1$ (GeV/c)^2
0.4
0.3
0.2
0.1
0
1
2
3
5
10
15
25
50
100
200
300
ω

FIG. 11

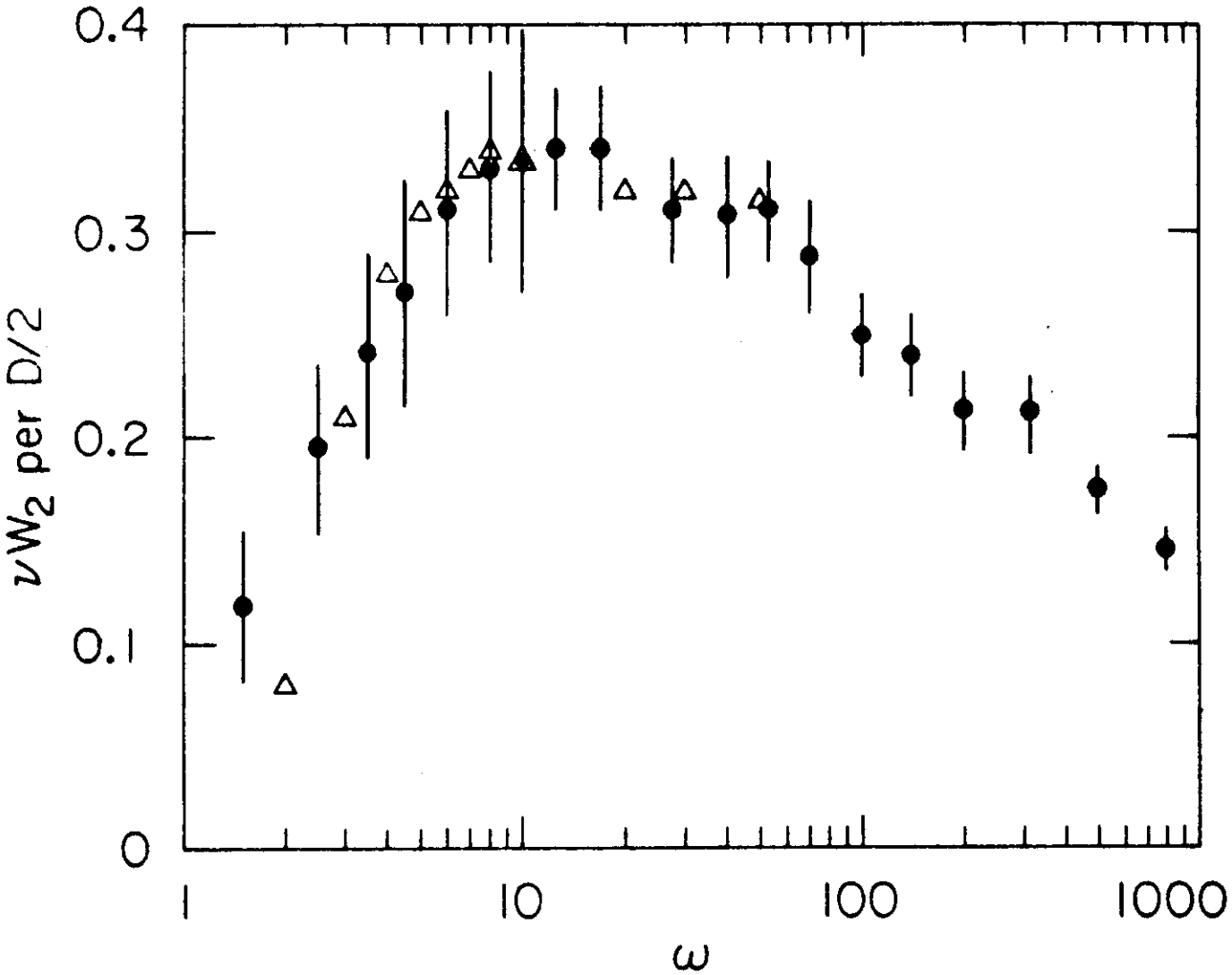

FIG. 12

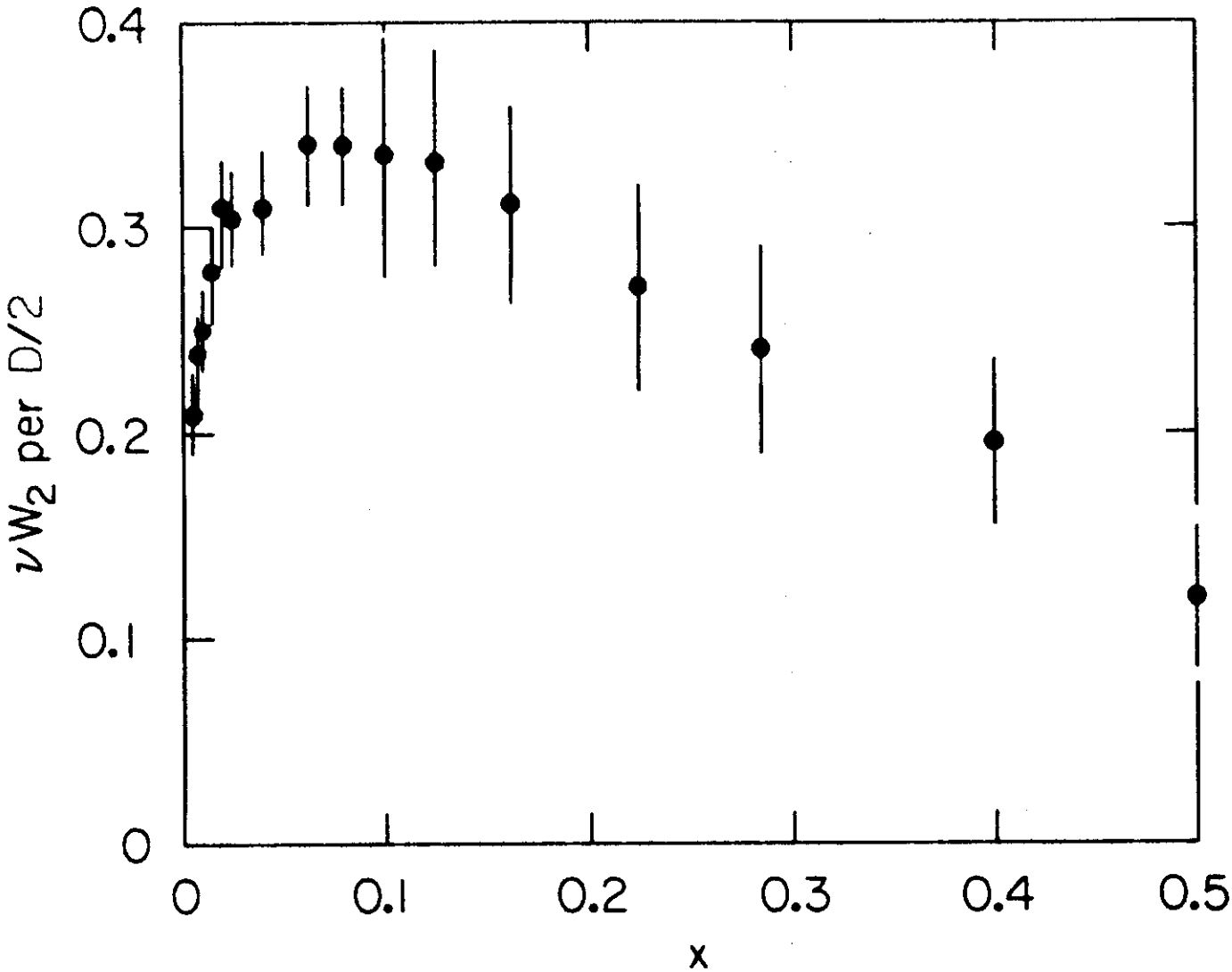

FIG. 13

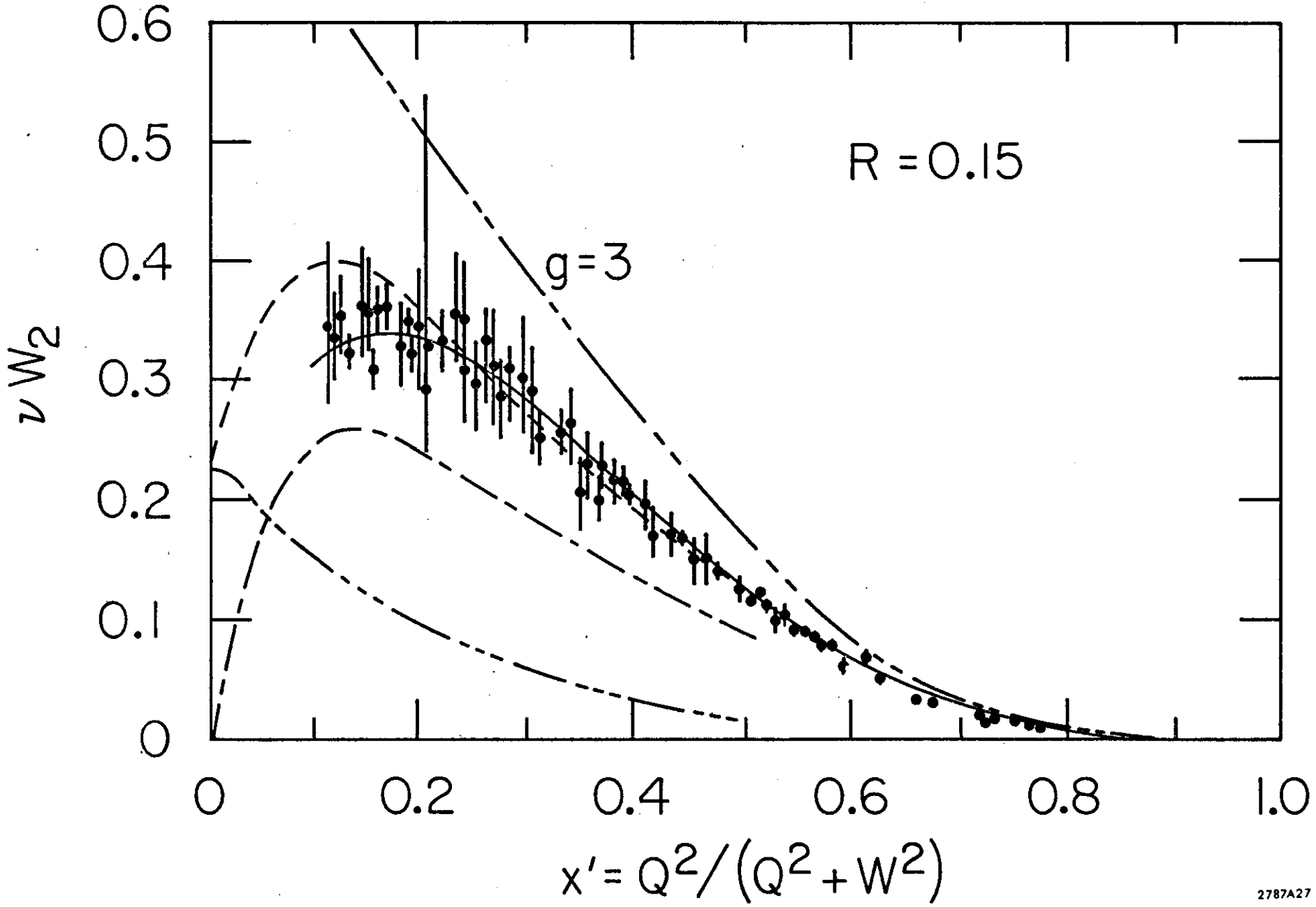

FIG. 14

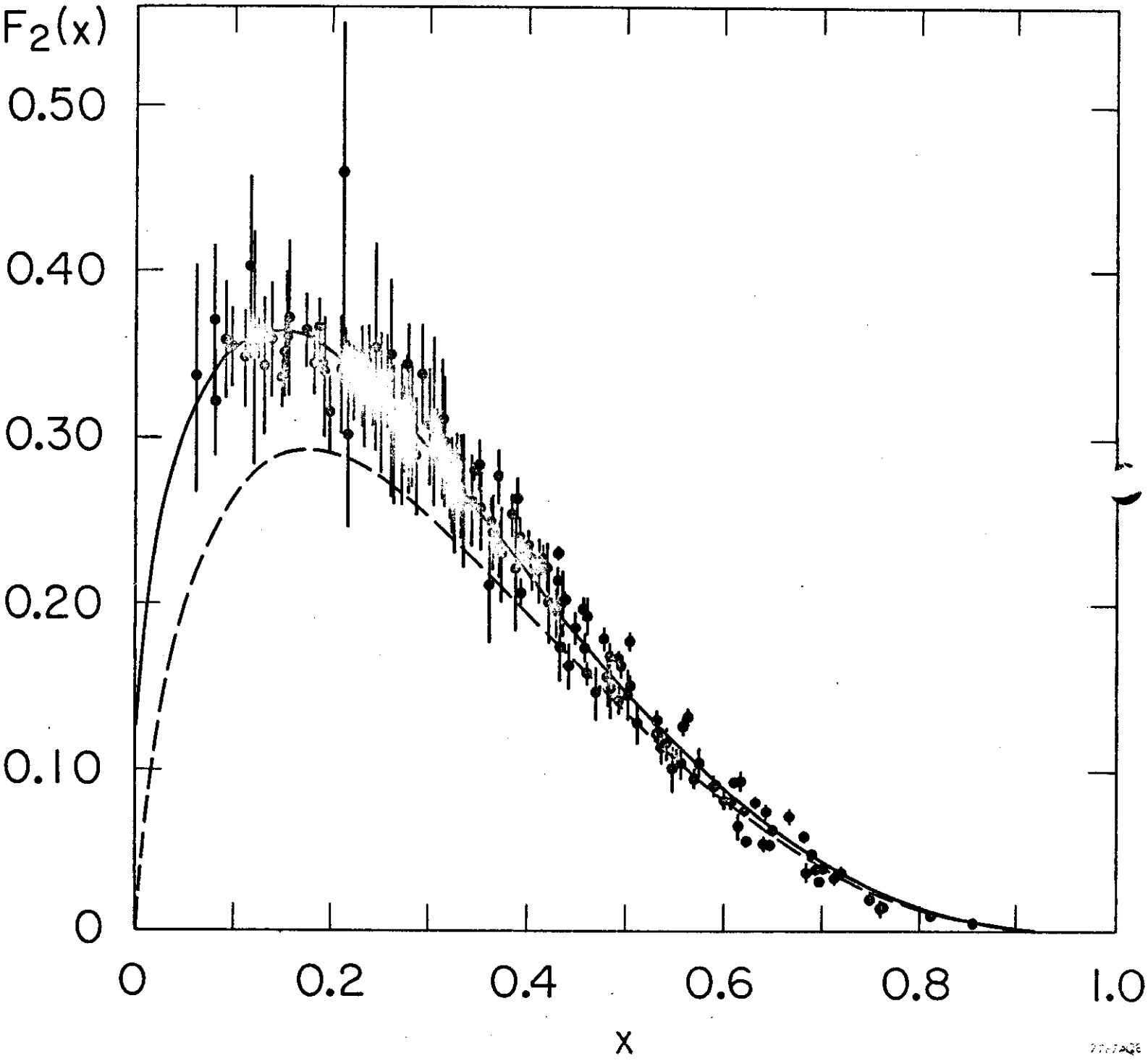

FIG. 15

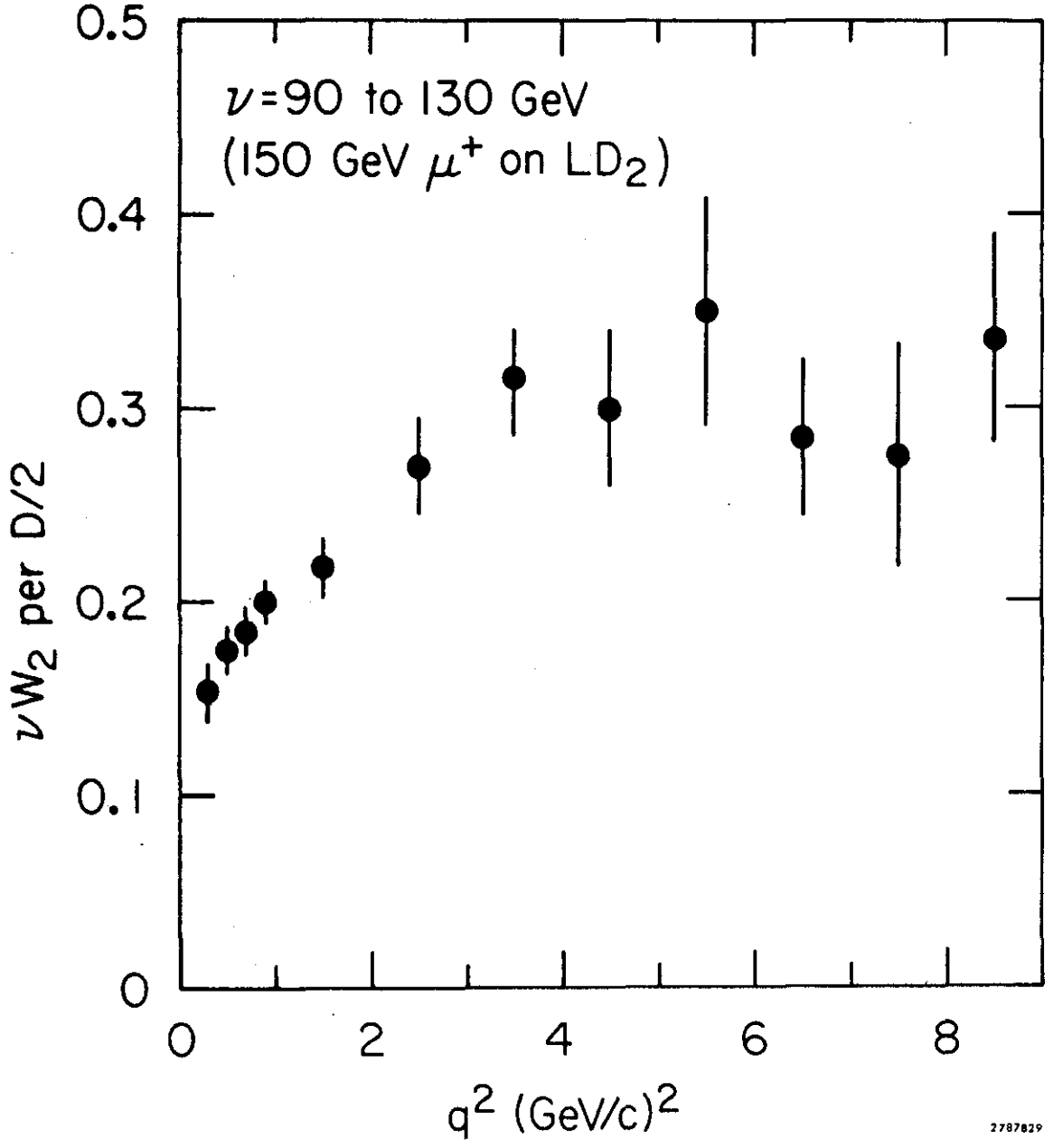
ν=90 to 130 GeV
(150 GeV μ^+ on LD_2)
0.5
0.4
0.3
0.2
0.1
0
νW_2 per D/2
0
2
4
6
8
q^2 (GeV/c)^2
2787829

FIG. 16

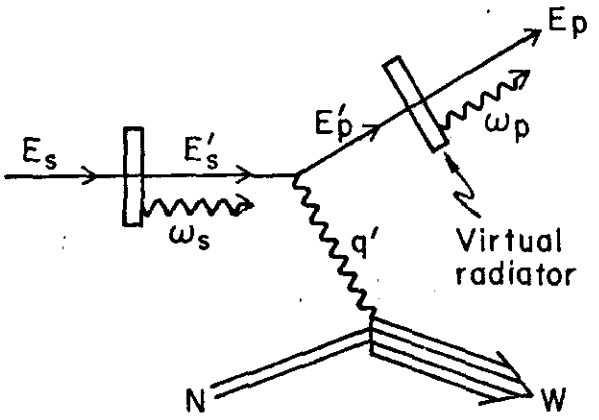
Ep
E'p
ωp
Es
E's
ωs
q'
Virtual
radiator
N
W

(a)

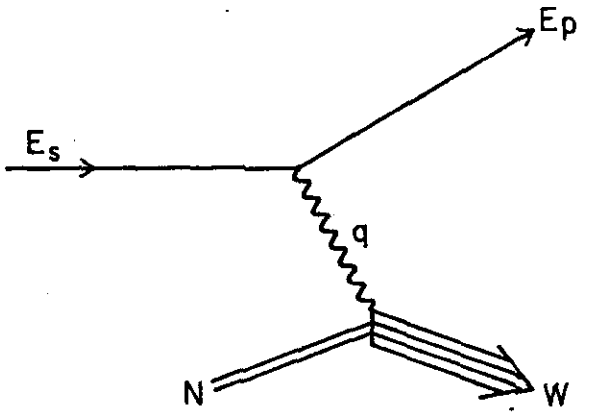
Ep
Es
q
N
W

(b)

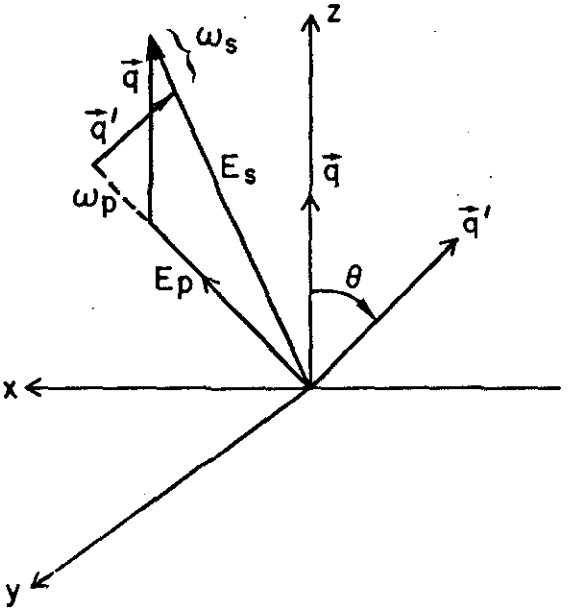
ωs
z
q
q'
Es
q
ωp
q'
Ep
θ
x
y

(c)

FIG. 17

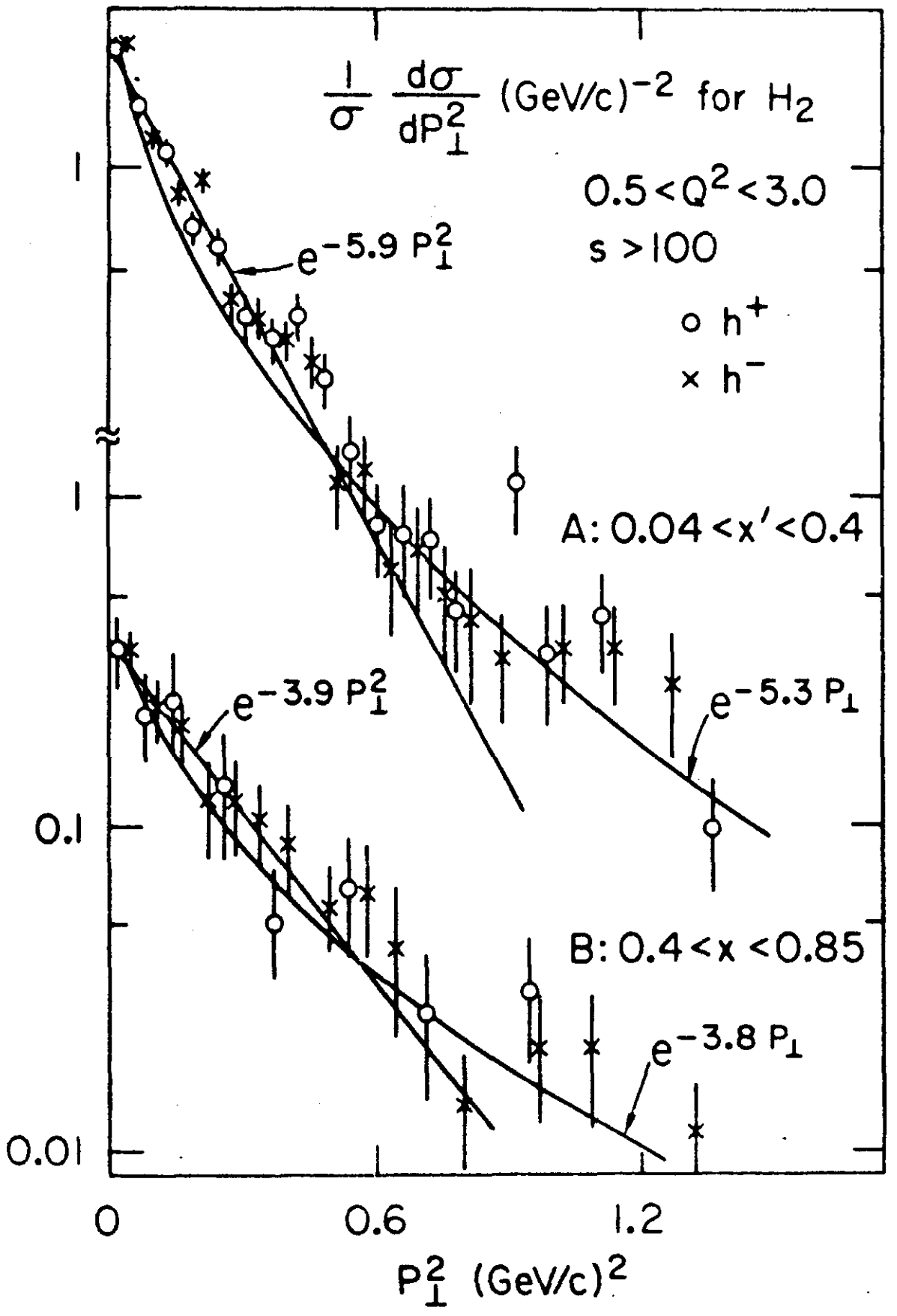
$\frac{1}{\sigma}\frac{d\sigma}{dP_\perp^2}$ (GeV/c)$^{-2}$ for H_2
$0.5<Q^2<3.0$
$s>100$
o h^+
× h^-
$e^{-5.9\,P_\perp^2}$
A: $0.04<x'<0.4$
$e^{-3.9\,P_\perp^2}$
$e^{-5.3\,P_\perp}$
B: $0.4<x<0.85$
$e^{-3.8\,P_\perp}$
1
1
0.1
0.01
0
0.6
1.2
$P_\perp^2$ (GeV/c)^2

FIG. 18

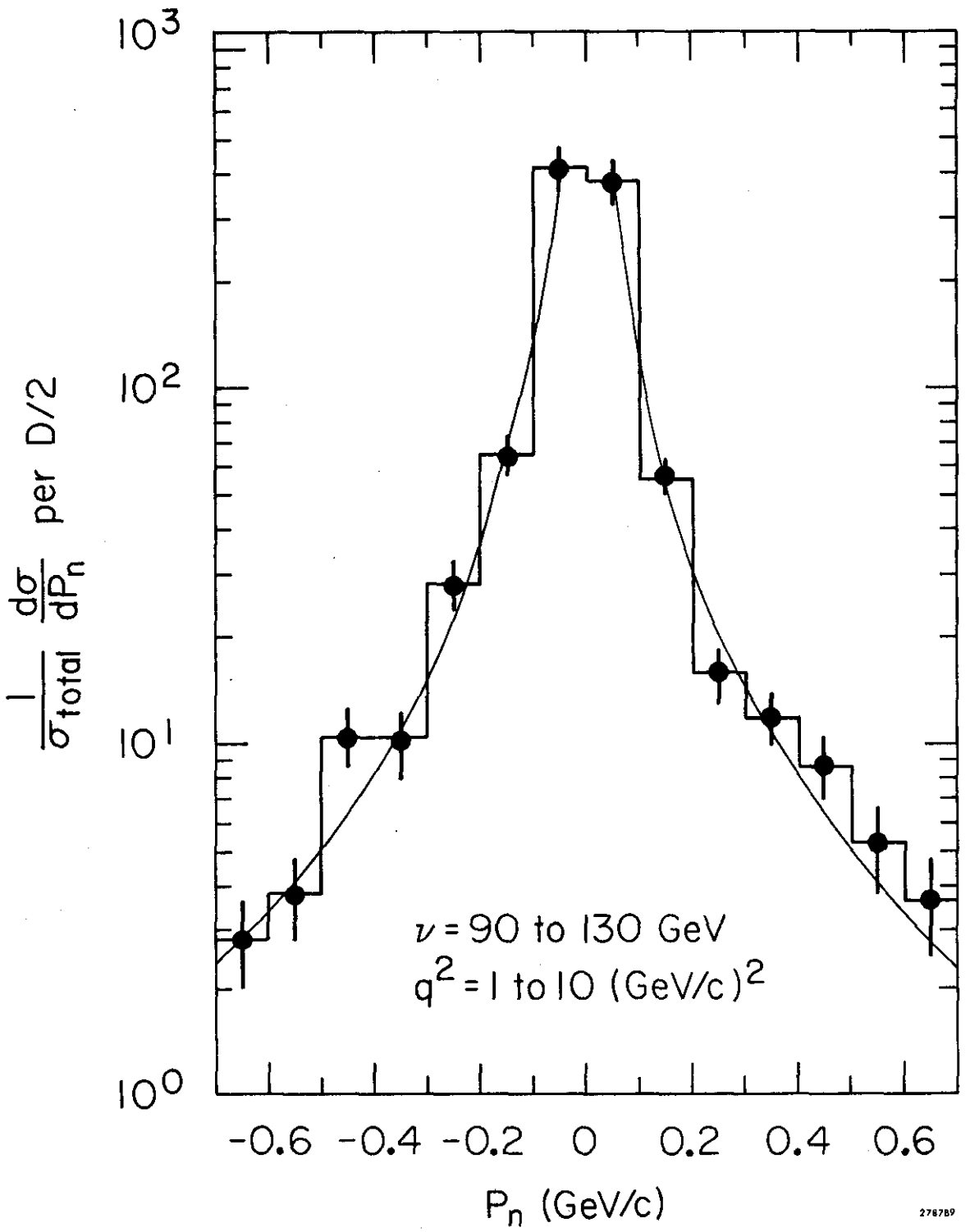
10^3
10^2
10^1
10^0
$\frac{1}{\sigma_{total}} \frac{d\sigma}{dP_n}$ per D/2
ν = 90 to 130 GeV
q^2 = 1 to 10 (GeV/c)^2
-0.6 -0.4 -0.2 0 0.2 0.4 0.6
P_n (GeV/c)
2787B9

FIG. 19

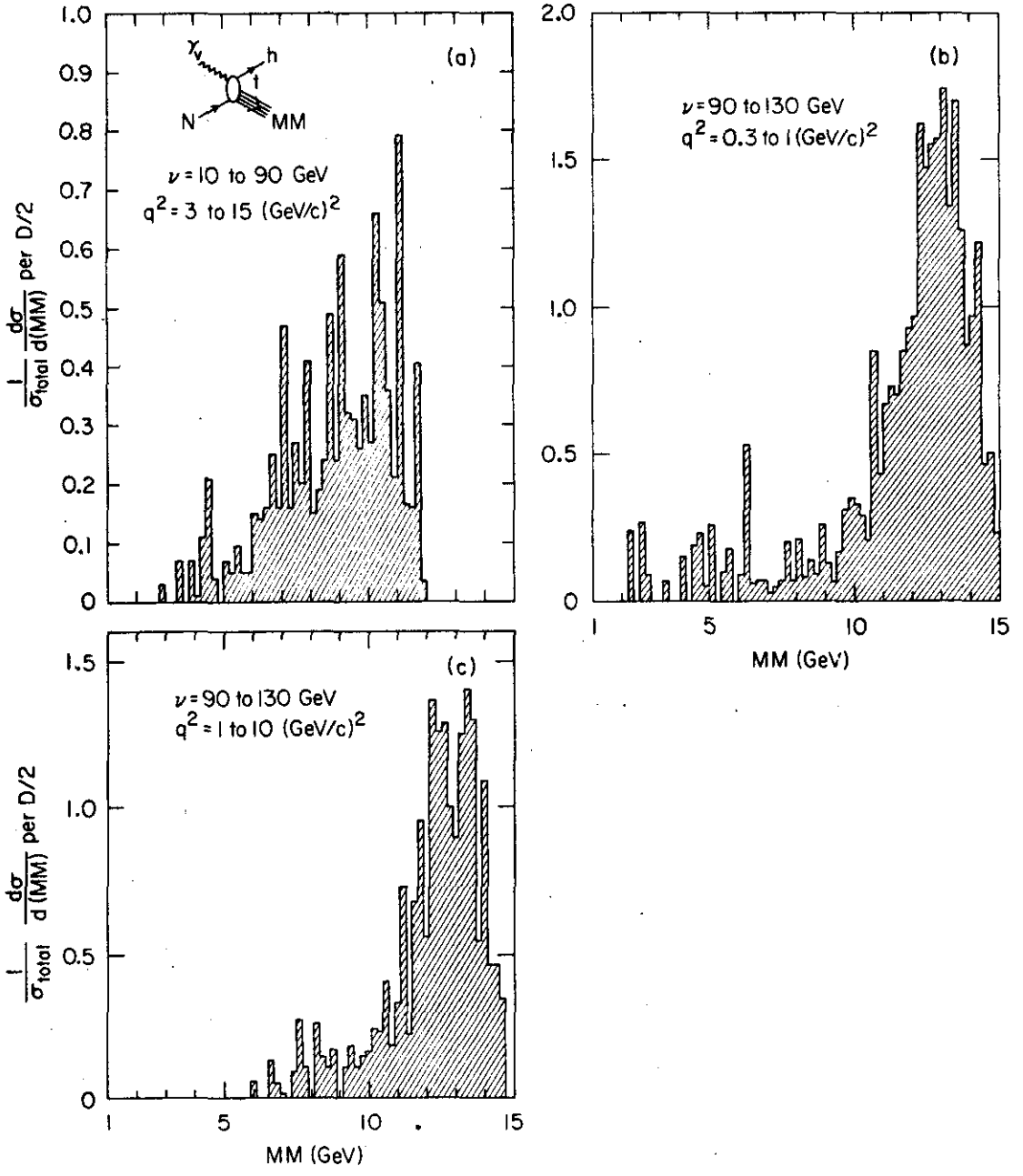
(a)
ν = 10 to 90 GeV
q^2 = 3 to 15 (GeV/c)^2
(b)
ν = 90 to 130 GeV
q^2 = 0.3 to 1 (GeV/c)^2
(c)
ν = 90 to 130 GeV
q^2 = 1 to 10 (GeV/c)^2
$\frac{1}{\sigma_{total}} \frac{d\sigma}{d(MM)}$ per D/2
MM (GeV)
N
MM
h

FIG. 20

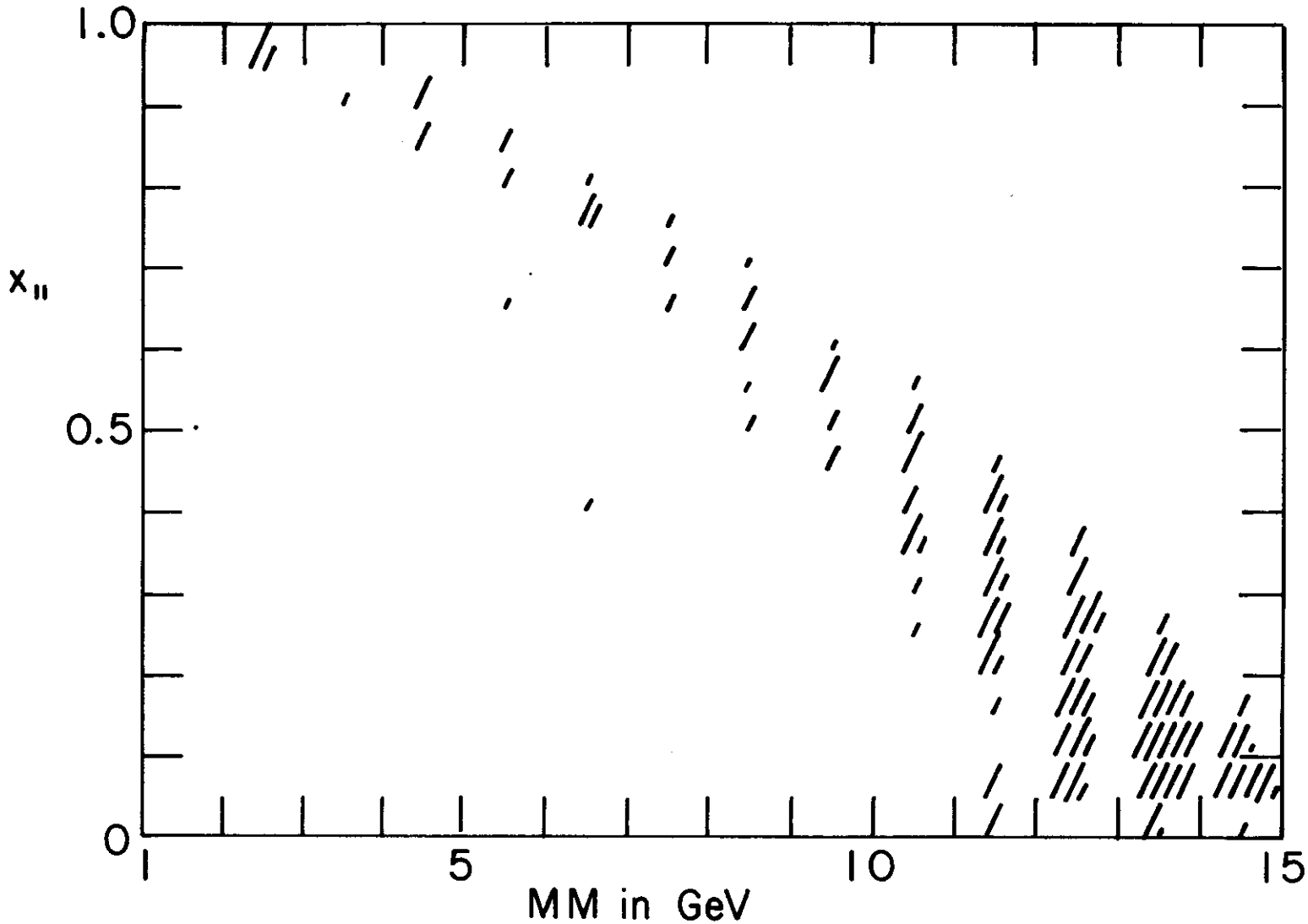

FIG. 21

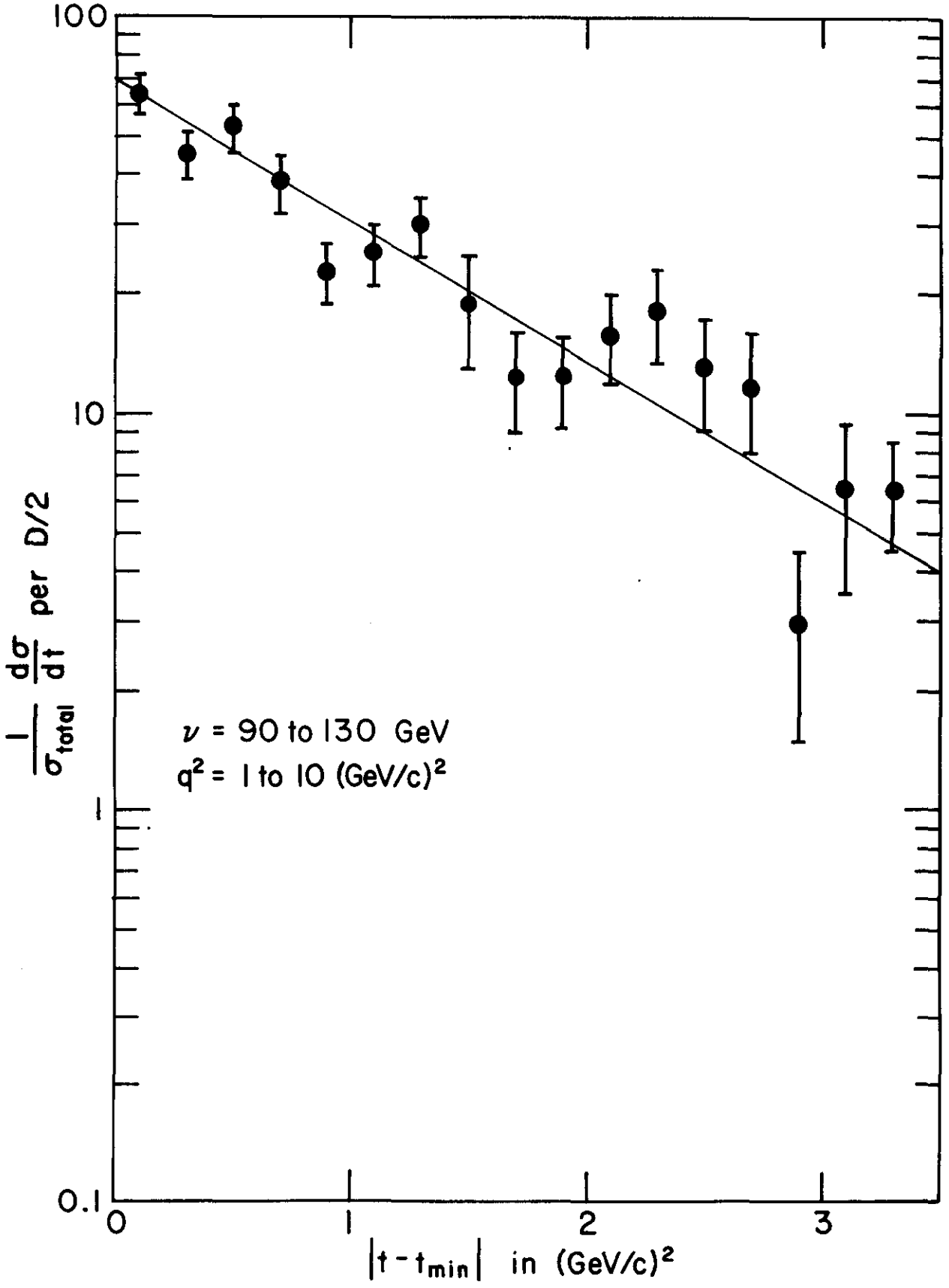
100
10
1
0.1
0
1
2
3
$\frac{1}{\sigma_{total}} \frac{d\sigma}{dt}$ per D/2
ν = 90 to 130 GeV
q^2 = 1 to 10 (GeV/c)^2
$|t - t_{min}|$ in (GeV/c)^2

FIG. 22

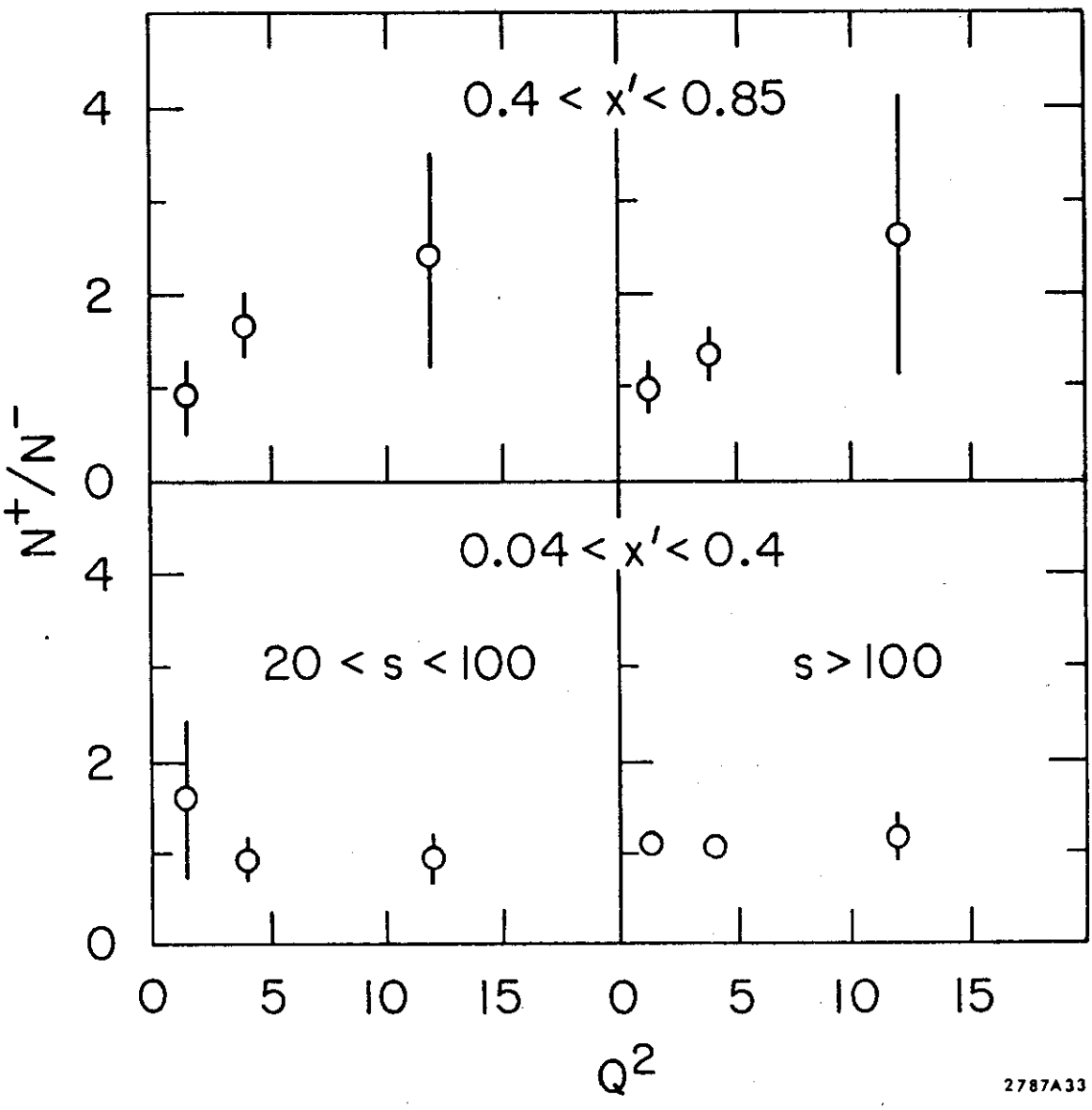

FIG. 23

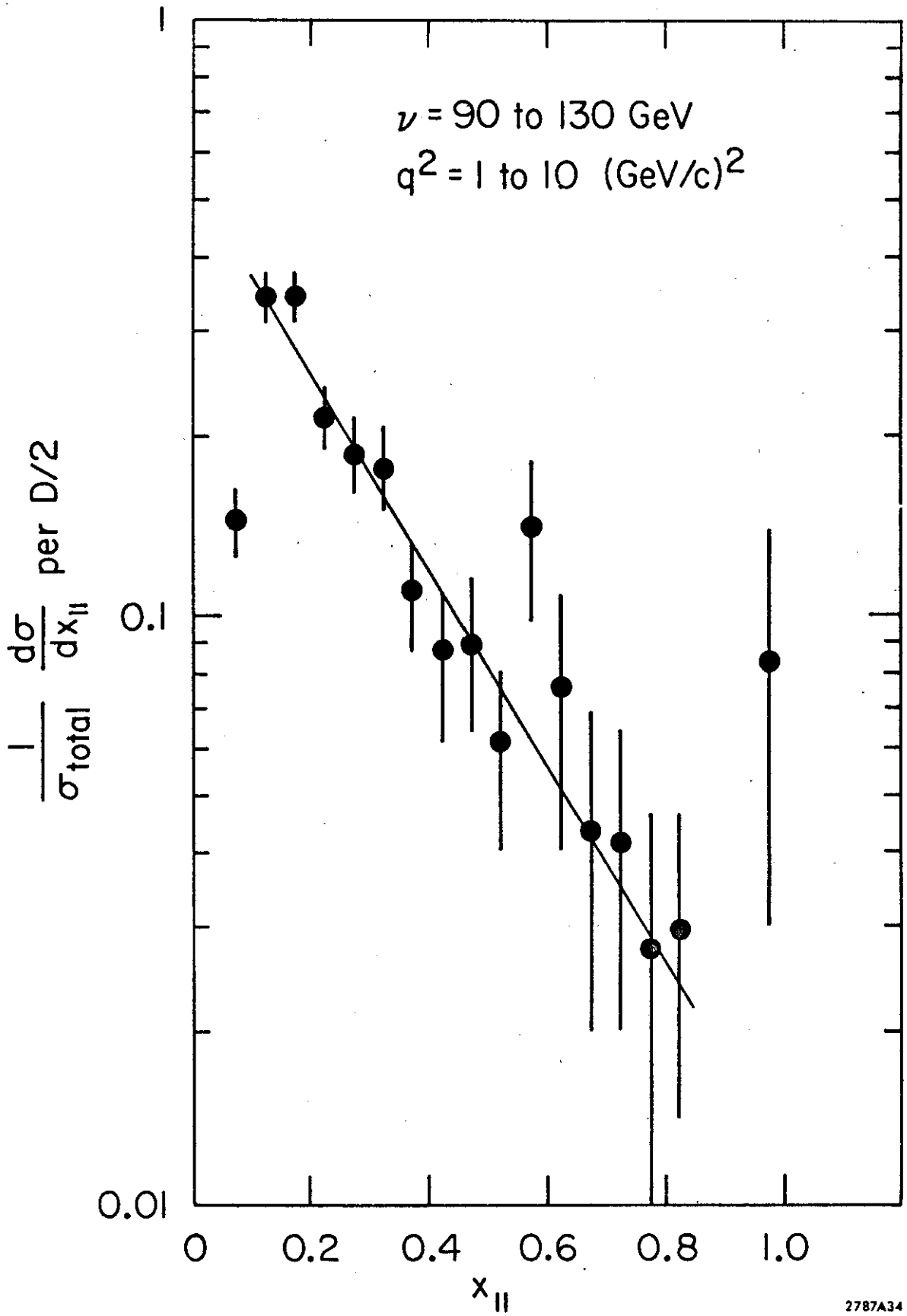
ν = 90 to 130 GeV
q^2 = 1 to 10 (GeV/c)^2
$\frac{1}{\sigma_{total}} \frac{d\sigma}{dx_{\parallel}}$ per D/2
1
0.1
0.01
0
0.2
0.4
0.6
0.8
1.0
$x_{\parallel}$
2787A34

FIG. 24

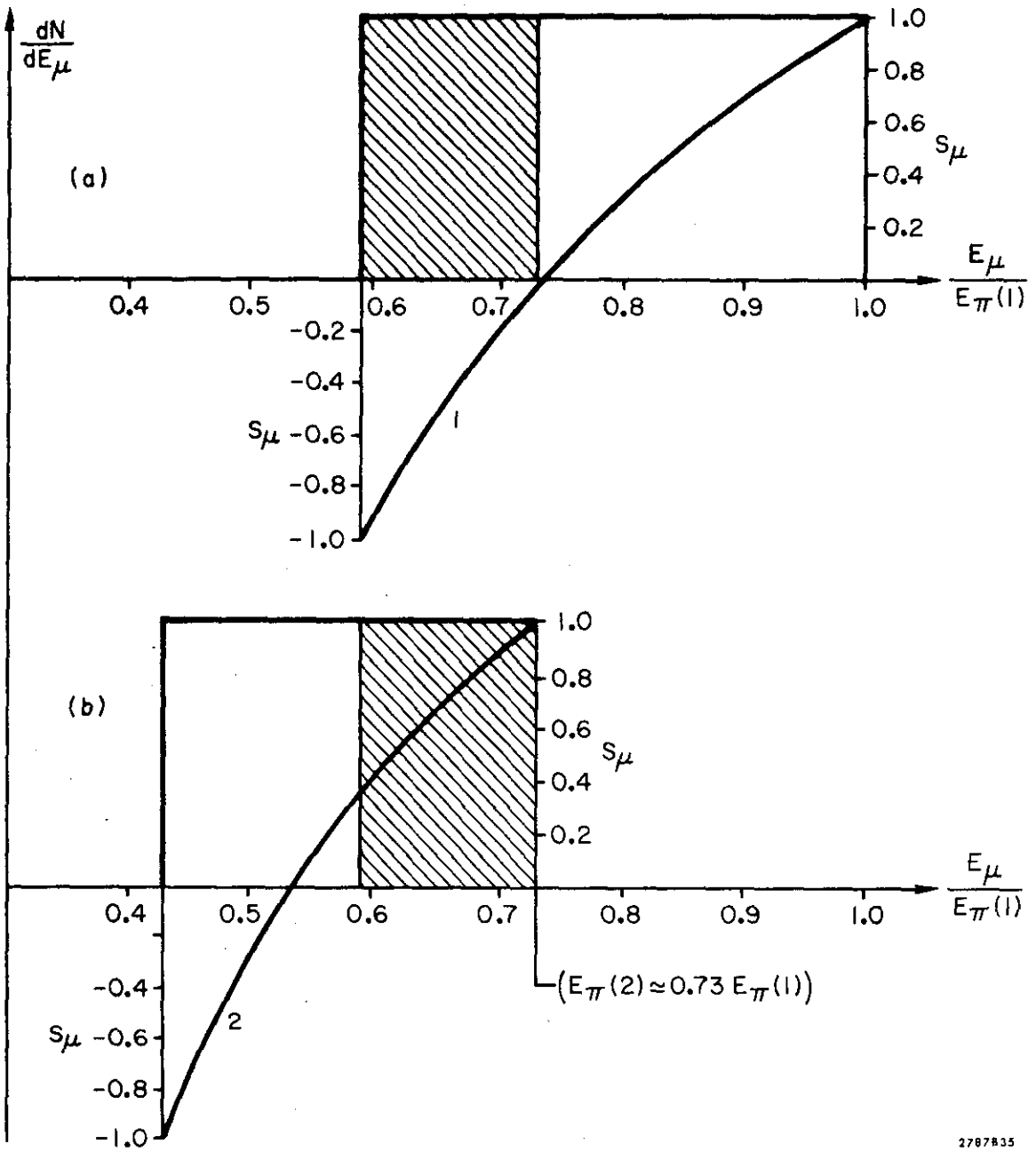
dN/dEμ
(a)
1.0
0.8
0.6
0.4
0.2
Sμ
Eμ/Eπ(1)
0.4
0.5
0.6
0.7
0.8
0.9
1.0
-0.2
-0.4
-0.6
-0.8
-1.0
1
(b)
(Eπ(2) ≃ 0.73 Eπ(1))
2
2787835

FIG. 25

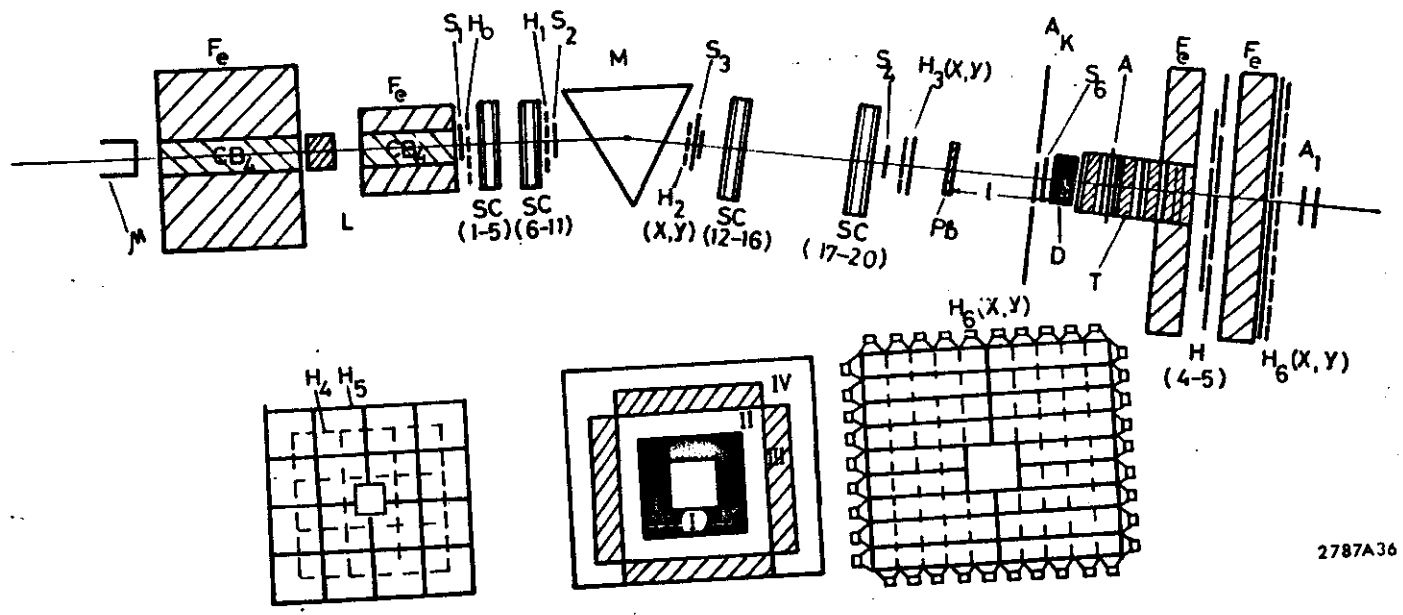
Fe
CB4
M
L
Fe
CB4
S1 H0
H1 S2
SC (1-5)
SC (6-11)
M
S3
H2 (X,Y)
SC (12-16)
SC (17-20)
S2
H3(X,Y)
Pb
I
AK
S6
A
D
T
Fe
Fe
A1
H6(X,Y)
H (4-5)
H6(X,Y)
H4 H5
IV
II
III
I
2787A36

FIG. 26

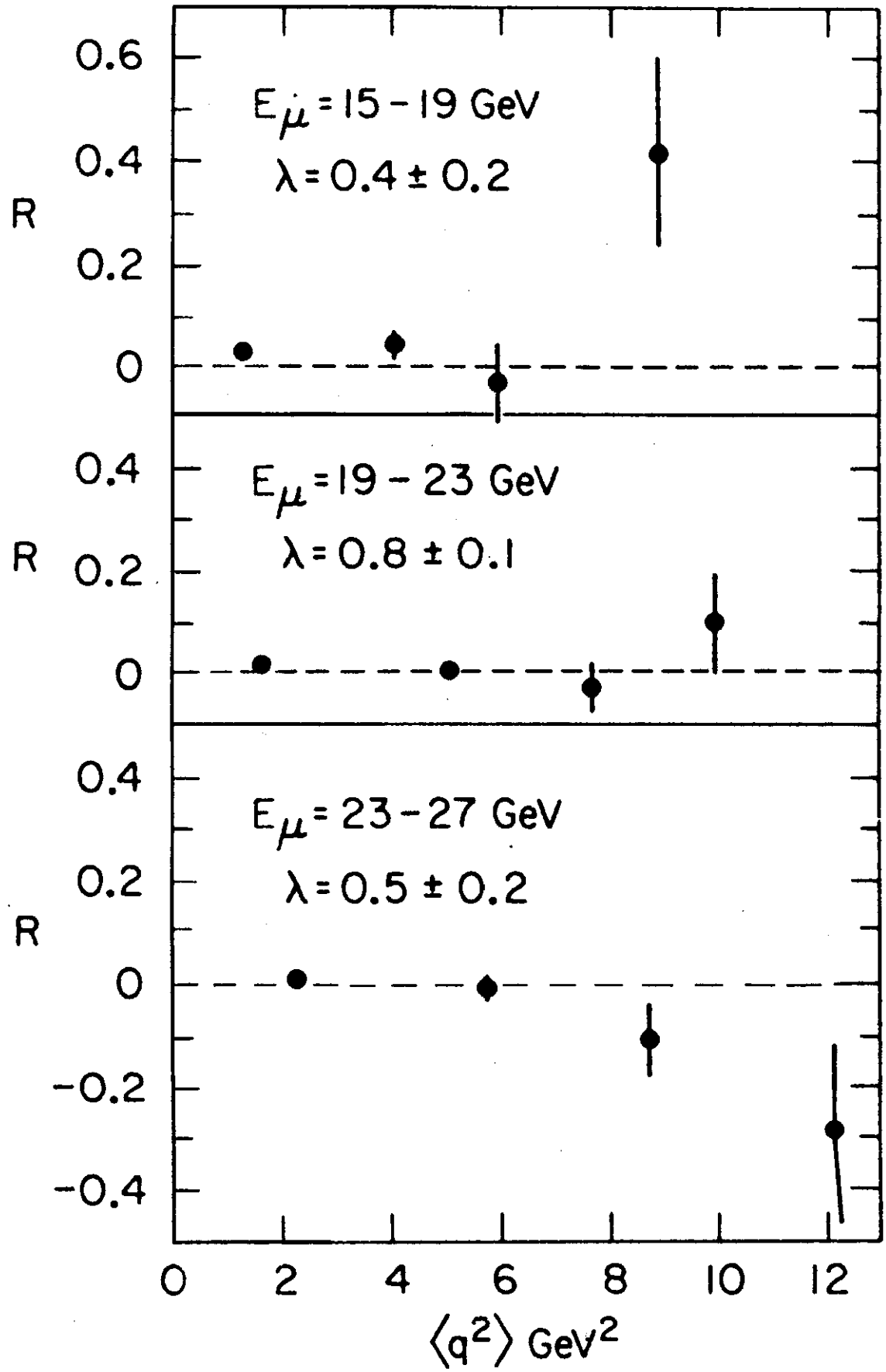
0.6
0.4
0.2
0
R
E_μ = 15 - 19 GeV
λ = 0.4 ± 0.2
0.4
0.2
0
R
E_μ = 19 - 23 GeV
λ = 0.8 ± 0.1
0.4
0.2
0
-0.2
-0.4
R
E_μ = 23 - 27 GeV
λ = 0.5 ± 0.2
0
2
4
6
8
10
12
$\langle q^2 \rangle$ GeV^2

FIG. 27